Site-Specific Nanobody Inhibitors of the Proteasomal Deubiquitinase UCH37

Yanfeng Li, Lin Hui Chang, Rishi Patel, Elizaveta I. Shestoperova, Jiale Du, Chittaranjan Das, Eric R. Strieter

Department of Chemistry, University of Massachusetts Amherst, Amherst MA 01003
Department of Chemistry, University of Massachusetts Amherst, Amherst MA 01003
Department of Chemistry, Purdue University, West Lafayette, IN 47907
Graduate program in Molecular & Cellular Biology, University of Massachusetts Amherst, Amherst MA 01003

ABSTRACT

Dysregulation of the ubiquitin (Ub) proteasome system (UPS) is linked to numerous human diseases, making its components, particularly deubiquitinases (DUBs), attractive therapeutic targets. UCH37 (also known as UCHL5), a proteasomal DUB, plays roles in protein degradation, DNA repair, and transcription and is overexpressed in several cancers. Despite its relevance, the precise functions of UCH37 within the proteasome and the INO80 chromatin remodeling complex remain unclear. Current small-molecule inhibitors exhibit broad, off-target effects, limiting their utility both therapeutically and as probes for UCH37 function. Here, we report the development of highly potent, selective nanobody-based inhibitors for UCH37. Using yeast surface display, we generated nanobodies targeting distinct Ub-binding sites on UCH37, with binding specificity confirmed by X-ray crystallography and hydrogen-deuterium exchange mass spectrometry. We find that the nanobody targeting the canonical Ub binding site serves as a pan-UCH37 inhibitor, while the one binding to the K48 chain-specific site selectively inhibits Ub chain debranching. Expression of this Ub chain debranching-specific nanobody in cells enabled identification of proteins whose degradation depends on UCH37. This work provides novel tools for investigating the biological functions of UCH37 and lays the groundwork for evaluating its potential as a therapeutic target.

INTRODUCTION

The ubiquitin-proteasome system (UPS) plays a fundamental role in human biology by selectively targeting proteins for degradation[1]. It is a critical regulator of key processes such as the cell cycle[2], transcription[3], DNA repair[4], and cellular responses to growth factors and stress[5,6]. Misregulation of the UPS is a hallmark of numerous human diseases, driving significant interest in developing therapeutic strategies to modulate its components[7–9]. Among these, deubiquitinases (DUBs)—the enzymes responsible for removing and editing ubiquitin modifications—are particularly attractive therapeutic targets due to their diversity and well-defined catalytic sites[10,11]. However, developing selective DUB inhibitors is often challenging, hindered by a lack of understanding of DUB biology and targets.

The challenge of developing selective inhibitors is especially relevant to the proteasomal deubiquitinase (DUB) UCHL5, also known as UCH37. UCH37 is a ubiquitously expressed DUB that is recruited to the distal portion of the 26S proteasome by the ubiquitin-binding subunit ADRM1/RPN13, and it also functions as a subunit of the INO80 chromatin remodeling complex[12–16]. Overexpression of UCH37 has been observed in several human cancers, including esophageal[17], ovarian[18], liver[19], colorectal[20], and gastric cancers[21]. In some cases, elevated levels of UCH37 have been linked to poor patient outcomes. However, the precise roles of UCH37 in the proteasome and the INO80 complex remain poorly understood, leaving the molecular basis for its association with pathogenesis unclear. Small-molecule inhibitors such as b-AP15 and VLX1570, based on a reactive α,β-unsaturated carbonyl motif, were developed primarily to target proteasome-associated deubiquitinases, including UCH37 and USP14, and have been evaluated in clinical trials[21–24]. Unfortunately, these molecules target a broad range of proteins, inducing nonspecific aggregation and general cellular toxicity[25,26]. As a result, the therapeutic potential of targeting UCH37 remains uncertain, and any conclusions drawn from using these molecules should be approached with caution.

We set out to develop a new generation of high-precision tools to interrogate UCH37 function, building on recent advances in its biochemical and structural characterization. Our lab, along with others, discovered that UCH37 not only removes small C-terminal fragments from ubiquitin (Ub) but also preferentially cleaves branched Ub chains containing K48 linkages, thereby promoting proteasomal degradation[27,28]. Structural studies revealed that UCH37 utilizes an aromatic-rich motif on the opposite face of the enzyme, relative to the canonical Ub-binding site, to specifically bind Ub chains with K48 linkages and remove branchpoints[29]. We hypothesized that site-specific inhibitors targeting either the canonical Ub-binding site or the K48-specific debranching site could provide deeper insights into the biology of UCH37. Here, we report the development of nanobody-based inhibitors that bind distinct sites on UCH37, revealing additional targets of the proteasome-bound form of the enzyme.

RESULTS

Generation of Nanobodies Targeting UCH37

We employed a yeast surface-display library of synthetic nanobodies to screen for site-specific binders of UCH37 (Figure 1a, Supplementary Figures 1a-e)[30]. Our initial focus was on identifying nanobodies that target the K48 ubiquitin (Ub) chain-specific binding site, responsible for UCH37's debranching activity. We hypothesized that blocking UCH37's canonical S1 Ub binding site would increase the likelihood of isolating nanobodies that bind to the aromatic-rich motif comprising the K48-specific site (Figure 1a). To achieve this, we conjugated Ub propargylamine (Ub-PA) to the active site cysteine of UCH37 in the presence of the DEUBAD domain of RPN13, its proteasomal binding partner[31,32]. The DEUBAD domain is known to prevent UCH37 dimerization and enhance its debranching activity[33]. The resulting Ub-UCH37•RPN13^{DEUBAD} complex was then exposed to the yeast display library (Figure 1c). Magnetic-activated cell sorting (MACS) was used to remove non-binders, followed by fluorescence-activated cell sorting (FACS) to identify cells expressing high levels of nanobodies (c-myc tag) and robust binding to Ub-UCH37•RPN13^{DEUBAD} (biotin tag) (Figure 1d).

After multiple rounds of sorting and sequencing, we identified an enriched clone, designated Nb-v1. Recombinant production and purification of Nb-v1 revealed a dissociation constant (K_d) of 0.3 nM with free UCH37 (Supplementary Figure 2b). Pulldown assays confirmed that transfected Nb-v1 efficiently precipitated UCH37 from cell lysates but did not co-elute with other UCH37-interacting partners, such as proteasomal subunits (Supplementary Figure 2d). To further improve its binding affinity, we generated a library of Nb-v1 variants through error-prone PCR and conducted further rounds of selection targeting UCH37 within the context of the proteasome.

Next-generation sequencing (NGS) of the sorted population revealed several variants with enhanced binding to proteasomes from wild-type (WT) cells but not from UCH37-knockout cells (Figures 1e-f). Purification and binding analysis identified a variant with four substitutions (Q1R, L80Q, H99Y, A109P) that selectively binds UCH37 on 26S proteasomes (Supplementary Figure 2d, Supplementary Table 2), which we termed the non-canonical S1 (Nb-ncS1) binder (see below).

We then incubated the yeast-displayed nanobody library with the biotinylated Ub-UCH37•RPN13^{DEUBAD} complexed with Nb-ncS1 to block the non-canonical K48 binding site, thereby increasing the likelihood of isolating nanobodies that bind the canonical S1 site (Figure 1b). After enriching the population and identifying a high-frequency clone (Nb-v2), we performed affinity maturation using error-prone PCR, similar to the process for generating Nb-ncS1. To screen for canonical S1 (cS1) site binders, we used both biotinylated Ub-UCH37•RPN13^{DEUBAD} and Flag-tagged UCH37•RPN13^{DEUBAD} complexes (Figure 1b). Binders to the cS1 site were expected

to interact only with Flag-tagged UCH37•RPN13^{DEUBAD}, as the biotinylated complex had its cS1 site blocked by Ub (Figures 1g-h). This approach identified three consensus mutations (L47F, T50I, K99R) that produce a highly selective binder for the canonical S1 site, designated as Nb-cS1 (Supplementary Table 2).

Nanobodies Bind UCH37 with High Affinity

Pull-down assays were conducted to confirm the site-specific binding of the selected nanobodies. HaloTag-fused Nb-cS1 and Nb-ncS1, each immobilized on a chloroalkane resin, successfully pulled down recombinantly expressed UCH37•RPN13^{DEUBAD} (Figure 2a). However, only Nb-ncS1 bound UCH37•RPN13^{DEUBAD} when the canonical S1 site was blocked by covalently attaching Ub to the active site cysteine (Figure 2a). These results indicate that the selection strategies were effective, with Nb-cS1 targeting the canonical Ub binding site and Nb-ncS1 engaging a distinct region outside the primary S1 site.

To quantify binding affinities, we used microscale thermophoresis (MST) and surface plasmon resonance (SPR). MST revealed that Nb-cS1 binds UCH37•RPN13^{DEUBAD} with a K_d of 0.2 μM (Figure 2b), while Nb-ncS1 exhibited a significantly higher affinity (K_d = 0.15 nM) (Supplementary Figure 2a). Although the concentrations of Nb-ncS1 and UCH37•RPN13^{DEUBAD} used in MST were outside the optimal range relative to the expected K_d, SPR confirmed a similar affinity for Nb-ncS1 binding to UCH37 alone, with a K_d of 0.125 nM (Figure 2c).

We also assessed the binding stoichiometry of the nanobody complexes using size-exclusion chromatography coupled with multi-angle light scattering (SEC-MALS) and native electrospray ionization mass spectrometry (ESI-MS). Upon incubation with Nb-ncS1 or Nb-cS1, the UCH37•RPN13^{DEUBAD} complex exhibited shifts in both retention time and molar mass by SEC-MALS (Figure 2d). The measured molar masses of the complexes with Nb-ncS1 and Nb-cS1 were 75 kDa and 69 kDa, respectively (Figure 2e), consistent with a 1:1 binding stoichiometry for each nanobody. However, the ~7 kDa discrepancy between the measured and theoretical mass for the Nb-ncS1 complex prompted further analysis by ESI-MS. Native mass spectrometry confirmed the formation of a well-defined 1:1 complex between UCH37•RPN13^{DEUBAD} and Nb-ncS1 (Figure 2f). Notably, native MS also showed that when the canonical S1 site was covalently occupied by Ub-PA, Nb-ncS1 still bound and formed a stable 1:1 complex with UCH37, consistent with its engagement at a distinct binding site.

Nanobodies Bind Distinct Sites on UCH37

Having identified high-affinity nanobodies, we next sought structural insights into their binding sites. We successfully solved the X-ray crystal structure of UCH37·RPN13^{DEUBAD} in complex with Nb-cS1 at a resolution of 2.40 Å (Figure 3a,

Supplementary Table 3). Superimposing this structure with the previously reported Ub-conjugated UCH37·RPN13^{DEUBAD} complex revealed that Nb-cS1 occupies the canonical S1 site, overlapping with the position of Ub (Figure 3b). In both complexes, UCH37 residue W36 plays a central role in binding: in the nanobody-bound structure, W36 is inserted into a hydrophobic pocket formed by Y37, I50, A96, I101, A104, and W106 of Nb-cS1 (Figure 3c), similar to how it is contacted by Ub in the previously reported structure[32]. Despite this shared interface, several conformational differences distinguish the Nb-cS1- and Ub-bound forms. Most notably, the C-terminal helical domain of UCH37 is tilted in the Nb-cS1-bound structure, and the loop containing residue I216—which contacts I36 of Ub—is flipped (Figure 3b). Additionally, the region encompassing residues 60–71 is poorly resolved in the Nb-cS1-bound structure (Figure 3b), suggesting increased flexibility. These conformational differences may have implications for how UCH37 accommodates and edits polyUb chains and raised the question of whether nanobody binding, like Ub, influences the enzyme's catalytic architecture.

In the apo form of UCH37, the catalytic cysteine C88 is misaligned with respect to other key residues, such as H164 and D179 (Supplementary Figure 3). Ub binding to the canonical S1 site induces a conformational rearrangement that brings C88 into proximity with H164 and D179 promoting catalytic competence[33]. Strikingly, the Nb-cS1-bound structure reveals that the nanobody similarly aligns the catalytic residues (Supplementary Figure 3), suggesting it stabilizes a catalytically competent conformation even in the absence of Ub.

To determine whether these crystallographic observations are preserved in solution, we used hydrogen-deuterium exchange mass spectrometry (HDX-MS) to compare the apo and Nb-cS1-bound forms of UCH37. The HDX-MS data revealed two regions of UCH37 with significantly reduced deuterium uptake upon Nb-cS1 binding (Figures 3d-e). The first, residues 32–43, includes W36—a key residue involved in binding both Ub and Nb-cS1—highlighting the shared engagement of this anchoring point. Functional relevance was confirmed by pulldown assays: mutating W36 to alanine (W36A) abolished binding to His-tagged Nb-cS1, whereas mutations in other ubiquitin-interacting regions—including I216E, which reduces Ub affinity in the S1 canonical binding site; F117A, which disrupts the K48 chain-specific backside interface; and K265A, located in a region of the ULD domain that undergoes faster hydrogen-deuterium exchange (see below; Figure 3d)—had no effect on Nb-cS1 binding (Figure 3f). The second protected region, spanning residues 79–92, encompasses the

catalytic cysteine C88, supporting the conclusion that Nb-cS1 stabilizes the active conformation of the catalytic site.

In addition to these protections, HDX-MS also revealed modest increases in deuterium uptake in other regions during the intermediate labeling times (Figure 3d). These include the final β-strand of the catalytic domain and the adjacent N-terminal segment of the C-terminal helical domain (residues 222–237), as well as a second region within the helical domain (residues 263–284). These increases suggest enhanced flexibility in parts of the C-terminal helical domain, consistent with the conformational changes observed in the crystal structure. Functionally, this conformational remodeling may influence how UCH37 interacts with polyUb chains and RPN13. Supporting the impact on RPN13, western blot analysis (see below; Figure 6b) shows reduced co-elution of RPN13 with Nb-cS1-bound UCH37, suggesting that nanobody binding could perturb the interaction between UCH37 and its regulatory partner.

Obtaining an atomic-level structure of Nb-ncS1 bound to UCH37 proved challenging due to crystallization difficulties. Nevertheless, HDX-MS provided valuable insights into the binding interface and associated conformational changes. The most pronounced reduction in deuterium exchange occurred in residues 114–135 (Figures 4a–b), corresponding to the K48-linked ubiquitin chain-specific binding site on the enzyme's backside. Outside this region, only minimal protection was observed at other known ubiquitin-binding surfaces, reinforcing the specificity of Nb-ncS1 for the backside interface. In addition, regions spanning residues 19–31, 55–74, and 200–218 showed moderate-to-strong protection, suggesting conformational stabilization of domains adjacent to the binding site. Together, these findings support a model in which Nb-ncS1 selectively engages the K48 chain-specific interface on the backside of UCH37.

AlphaFold modeling further corroborated our experimental observations. To investigate the interaction between Nb-ncS1 and UCH37, we initially modeled full-length UCH37 in complex with RPN13 and Nb-ncS1. However, these initial models yielded low-confidence interface scores (interface predicted TM-score, ipTM ≈ 0.2) and incorrectly placed Nb-ncS1 at the canonical S1 ubiquitin-binding site—an outcome inconsistent with our yeast display selection strategy (Figure 1) and binding data (Figure 2), both of which indicate that Nb-ncS1 engages a distinct, non-canonical site. To refine the model, we incorporated ubiquitin into the canonical S1 site to sterically bias the prediction away from this region. Upon inclusion of ubiquitin, Nb-ncS1 consistently bound the enzyme's backside across five independent models (Figure 4c), all exhibiting low predicted aligned error (PAE) (Supplementary Figure 4a) and high-confidence interface predictions. Notably, the ipTM scores for the Nb-ncS1–UCH37 interface exceeded 0.8 in all cases, indicating a robust and well-defined interaction in line with our HDX-MS data (Figure 4d). These models further predicted that complementarity-determining regions 1 and 3 (CDRs 1 and 3), but not CDR2,

mediate engagement of the backside surface, specifically contacting the K48 chain-specific motif centered on F117 and F121 of UCH37 (Figure 4f).

To experimentally test whether CDRs 1 and 3, but not CDR2, contact UCH37, we again employed HDX-MS to compare the bound and unbound forms of Nb-ncS1. The data revealed two regions with markedly reduced deuterium uptake upon binding: residues 19-29, which comprises CDR1, and residues 99-120, encompassing CDR3 (Figures 4e-f). In contrast, no significant protection was observed for residues 52-69 which comprise CDR2. Thus, in agreement with the AlphaFold prediction, only CDRs 1 and 3 appear to mediate binding to UCH37.

Finally, to validate that Nb-ncS1 engages the predicted backside surface of UCH37, we tested the impact of mutating F117 and F121—two key aromatic residues within the K48-specific motif. Pull-down assays revealed a marked reduction in Nb-ncS1 binding to the F117A/F121A UCH37 mutant, while binding of Nb-cS1 remained unaffected (Figure 4g). Consistent with these findings, native ESI-MS detected no Nb-ncS1-bound form of the mutant UCH37 (Supplementary Figure 4b). Together, these results confirm that Nb-ncS1 selectively targets the non-canonical K48-specific site on the backside of UCH37.

Nb-cS1 and Nb-ncS1 have Distinct Effects on UCH37

With the binding sites confirmed, we wanted to measure the effects on biochemical activities. Considering Nb-cS1 uses the canonical S1 Ub-binding site to engage UCH37, we surmised that it would interfere with the removal of small C-terminal Ub adducts while Nb-ncS1 would have little effect due to binding on the opposite face of the enzyme[32]. To test this, we examined the hydrolysis of Ub-aminomethylcoumarin (AMC) in the presence and absence of the nanobodies. As expected, the addition of Nb-cS1 significantly impairs Ub-AMC hydrolysis while Nb-ncS1 does not (Figure 5a). We also used Ub-propargylamine labeling as a secondary assay for validation. In this case, the C-terminal propargylamine adduct directly reacts with the active site cysteine of UCH37 forming a covalent Ub-UCH37 complex. Congruent with the results from the Ub-AMC assay, only Nb-cS1 exhibited significant inhibition (Figure 5b).

Next, we sought to evaluate the impact of nanobodies on Ub chain binding. As we have previously shown, the non-canonical S1 (nc-S1) site located on the backside of UCH37 is necessary for binding K48-linked Ub chains[29]. Thus, not surprisingly, we found that Nb-ncS1 abolishes the binding of both unbranched and branched K48 chains in pull-down assays (Figure 5c). Nb-cS1 also diminished the binding of chains, but the effect was more pronounced for branched chains relative to unbranched chains. Work from our lab and others has demonstrated that the non-K48 linked Ub subunit of a branched chain forms contacts with UCH37. It is likely these interactions overlap with the Nb-cS1 binding site, suggesting how the nanobody interferes with chain

binding. Alternatively, as the crystal structure and HDX-MS data suggest, binding of Nb-cS1 to the canonical Ub-binding site could promote a conformation of UCH37 that might no longer be conducive to chain binding.

Since Nb-ncS1 and Nb-cS1 interfere with ubiquitin chain binding, we reasoned that each nanobody would also impede chain debranching. To test this, we added the nanobodies to reactions containing either model branched tri-ubiquitin substrates or enzymatically derived high–molecular weight (HMW) ubiquitin conjugates bearing branchpoints. Reactions were monitored by gel electrophoresis to detect the formation of lower–molecular weight ubiquitin conjugates, and by middle-down mass spectrometry to specifically assess the impact on branchpoints. Across these complementary approaches, we found that both Nb-ncS1 and Nb-cS1 inhibit chain debranching (Figures 5d–e, Supplementary Figure 5a–f). More detailed quantitative analysis was performed for Nb-ncS1. Steady-state kinetic analysis of the debranching reaction using K6/K48-linked Ub_3 revealed that Nb-ncS1 acts as a competitive inhibitor, with a K_i of 120 nM (Figure 5f). The ~800-fold discrepancy between its binding affinity ($K_d \approx 0.15$ nM) and inhibitory constant is striking but can be explained by the fact that Nb-ncS1 selectively occludes only one of the Ub-binding sites on UCH37—specifically the K48-binding site—while leaving other Ub-recognition surfaces required for engaging branched chains intact. These findings support a model in which Nb-ncS1 interferes with a specific mode of Ub chain recognition necessary for debranching, without fully obstructing the catalytic core. In contrast, Nb-cS1 impairs both debranching and C-terminal hydrolase activity.

Nb-ncS1 and Nb-cS1 Selectively Engage UCH37 in Cells

The use of Nb-ncS1 and Nb-cS1 as inhibitors of UCH37 requires that each nanobody selectively engage its target in cells. Before assessing proteome-wide selectivity, we first evaluated whether Nb-ncS1 and Nb-cS1 interact with UCH37 in a cellular context. HEK293FT wild-type (WT) and UCH37 knockout (UCH37KO) cells were transiently transfected with HA-Flag-tagged versions of Nb-ncS1, Nb-cS1, or a control nanobody (Nb-ctrl) (Figure 6a). Following immunoprecipitation, western blot analysis showed that Nb-ncS1 efficiently pulled down endogenous UCH37 from WT cells, along with proteasomal subunits including RPN13 (19S), RPN11 (19S), RPT2 (19S), and PSMA2 (20S) (Figure 6b). In contrast, while Nb-cS1 also co-immunoprecipitated UCH37, the amount recovered was substantially lower, consistent with a weaker binding interaction. Correspondingly, only trace amounts of RPN13 were detected, and no other proteasomal subunits were co-purified with Nb-cS1. No enrichment of UCH37 or

other proteasomal components was observed from UCH37KO cells or when Nb-ctrl was used instead of Nb-ncS1 and Nb-cS1.

To further probe cellular engagement, we employed a proximity ligation assay (PLA)[35]. In doing so, intracellular interactions between UCH37 and Nb-ncS1 or Nb-cS1 can be transformed into an amplifiable signal with oligonucleotide-labeled antibodies and rolling circle DNA replication. The signal is then detected by fluorescence microscopy using fluorescently-labeled oligonucleotides that bind to the amplified sequences. In HEK293FT cells expressing HA-Flag-tagged Nb-ncS1 or Nb-cS1, fluorescent puncta are observed upon the addition of antibodies that recognize UCH37 and the HA tag fused to the nanobodies (Figure 6c). By contrast, markedly fewer puncta are observed using the anti-HA antibody along with an antibody that recognizes UCHL3, another DUB in the same UCH sub-family as UCH37. Likewise, the expression of Nb-ctrl, which does not bind UCH37, also affords few puncta. Together with the pulldown data, these results demonstrate that Nb-ncS1 and Nb-cS1 interact with UCH37 in cells.

Having demonstrated cellular engagement, we sought to assess selectivity on a proteome-wide scale. The nanobodies were transiently expressed as Halo-tag fusions. Immunoprecipitation followed by mass spectrometry (IP-MS) analysis was then performed to identify interacting partners. In WT cells, the data revealed that UCHL5/UCH37 was indeed the most enriched target of Halo-Nb-ncS1 and Halo-Nb-cS1 relative to Halo-Nb-ctrl (Figures 6d-e). A significant number of 19S and 20S proteasome subunits were also identified, consistent with western blot analysis. Conversely, fewer proteasome subunits were detected in the Halo-Nb-cS1 immunoprecipitation (Figure 6e), while more ribosomal proteins were enriched—a pattern not observed in the Nb-ncS1 immunoprecipitation (Figure 6d). In UCH37KO cells, we did not detect enrichment of any proteasome components, indicating that UCH37 is required for both Halo-Nb-ncS1 and Halo-Nb-cS1 to associate with the proteasome (Supplemental Figures 5a–b).

One possible explanation for the reduced recovery of proteasomal proteins with Halo-Nb-cS1 compared to Halo-Nb-ncS1 is that the population of UCH37 captured by Nb-cS1 is not complexed with RPN13. Previous studies have shown that deletion of full-length RPN13 reduces UCH37 protein levels, consistent with a stabilizing role for RPN13. If the UCH37–RPN13 interaction is initiated co-translationally, it is plausible that Nb-cS1 binds and stabilizes nascent UCH37 prior to complex formation. This model would be consistent with the enrichment of ribosomal proteins and the reduced recovery of RPN13 and other proteasomal subunits in the Nb-cS1 IP-MS dataset.

An alternative—and perhaps more likely—explanation is that Halo-Nb-cS1 is misfolded in human cells and therefore engages quality control machinery at the ribosome. In contrast to Halo-Nb-ncS1, which failed to enrich any proteins in UCH37KO cells, Halo-Nb-cS1 pulled down several proteins in the absence of UCH37,

including the translation elongation factor EEF2 and the HSP70 chaperone HSPA1B. These interactions suggest that Halo-Nb-cS1 may behave aberrantly during translation and require chaperone engagement. Despite these differences, both nanobodies exhibited selectivity toward UCH37 in HEK293FT cells; however, the superior specificity and cleaner proteomic profile of Nb-ncS1 indicate that it is the more reliable tool for probing UCH37 function in cells.

Nb-ncS1 Elevates the Levels of Short-lived Proteins

Previous efforts to identify proteins whose degradation is regulated by UCH37 relied on the expression of variants defective in Ub chain debranching[29]. While several putative substrate proteins were identified, debranching-specific inhibitors such as Nb-ncS1 potentially offer a more straightforward approach that can be employed in many biological paradigms. Thus, we sought to exploit Nb-ncS1 for the identification of proteins regulated by UCH37 to better define its role in proteostasis.

If UCH37-mediated chain debranching promotes the degradation of a subset of proteins, we reasoned that impairment of either debranching or the proteasome should lead to the accumulation of a similar set of proteins. Tandem mass tag (TMT)-based quantitative proteomics were performed to test this hypothesis. HEK293FT cells were transfected with either Halo-Nb-ctrl or Halo-Nb-ncS1, followed by treatment with H_2O_2, as UCH37 has been implicated in the cellular response to oxidative stress[36]. In parallel, oxidatively stressed HEK293FT cells expressing Halo-Nb-ctrl were treated with the proteasome inhibitor bortezomib (Btz). Mass spectrometry identified 2,909 proteins, applying a filter of at least two unique peptides per protein. Of the 2909 proteins identified, 20 were up-regulated under Btz treatment (based on $\log_2>0.5$). Of the 20 up-regulated by Btz, 3 were also up-regulated in cells expressing Nb-ncS1 (red data points; Figure 7). The degree of up-regulation is modest in comparison to Btz; however, this is not entirely unexpected since Ub chain editing by UCH37 is likely to fine tune degradation rates, not completely inhibit the process like Btz.

The proteins significantly up-regulated by Nb-ncS1 include chromatin modifiers (MRFAP1, MORF4L2) and scaffolding components (MAGED1). Under Btz treatment, additional proteins are up-regulated—transcriptional regulators (ZNF503, ZNF703) and cytoskeletal components (MZT2B, ZWINT, and β-catenin/CTNNB1)—which also show an upward trend, though not statistically significant, under Nb-ncS1 treatment. What these proteins all have in common is a short half-life[37]. Significantly fewer proteins are downregulated by Nb-ncS1, consistent with the model that Ub chain debranching by UCH37 promotes proteasomal degradation[27].

To validate some of the hits from TMT proteomics, we focused on the two short-lived proteins MRFAP1 and MORF4L2. Western blot analysis showed increased expression of both MRFAP1 and MORF4L2 upon transfection of Nb-ncS1 in HEK293FT WT cells. In HEK293FT UCH37 KO cells, however, the effect of Nb-ncS1 was substantially

muted, corroborating the TMT proteomic data. To then assess whether UCH37 regulates the degradation of MRFAP1 and MORF4L2, we examined the depletion of both proteins after shutting off translation in WT and UCH37 KO cells. We found that the loss of UCH37 reduces but does not abolish degradation. Our data demonstrate that Nb-ncS1 can be used to uncover proteins whose degradation depends on UCH37.

DISCUSSION

This study demonstrates the development of nanobodies (Nb-cS1 and Nb-ncS1) that selectively inhibit the proteasomal DUB UCH37 by targeting distinct binding sites. These inhibitors provide new tools to study UCH37's specific roles in ubiquitin chain processing, with implications for understanding proteasome function and proteostasis regulation.

We have shown that Nb-cS1 binds to the canonical S1 site of UCH37, effectively blocking both C-terminal ubiquitin (Ub) hydrolysis and chain debranching activities. In contrast, Nb-ncS1 binds to the non-canonical S1 (ncS1) site specific for K48-linked Ub chains, selectively impairing chain debranching. These results support the hypothesis that UCH37 uses distinct structural features for its multifaceted roles in Ub processing.

Interestingly, Nb-ncS1, while tightly binding to UCH37, did not inhibit C-terminal Ub hydrolysis, highlighting the spatial separation of UCH37's functional domains. This specificity could be crucial for therapeutic targeting, as selective inhibitors might spare certain UCH37 activities while still impairing its ability to regulate degradation pathways associated with Ub chain debranching. This is particularly relevant given the challenge of achieving selectivity when targeting deubiquitinases (DUBs), many of which share conserved catalytic motifs[38]. Our nanobody-based approach offers an avenue to design more precise inhibitors.

In cellular assays, Nb-ncS1 consistently demonstrated greater potency and selectivity for UCH37 than Nb-cS1. Quantitative IP-MS revealed that Nb-ncS1 enriches UCH37 more robustly than Nb-cS1, with minimal off-target binding, suggesting tighter and more specific engagement in cells. These findings are consistent with our biochemical analyses, which showed that Nb-ncS1 has higher affinity for UCH37 and selectively impairs chain debranching without broadly inhibiting other DUBs. In contrast, Nb-cS1 exhibited weaker cellular enrichment of UCH37 and modest off-target interactions, likely reflecting its lower binding affinity and broader inhibitory profile. Together, these data indicate that Nb-ncS1 is a more effective and selective tool for probing UCH37 function in the context of the proteasome and cellular proteostasis.

Our proteomic analyses revealed that UCH37 regulates the stability of a distinct subset of short-lived proteins involved in transcriptional control, chromatin remodeling, and cytoskeletal organization. The accumulation of factors such as MRFAP1, MORF4L2, and β-catenin upon Nb-ncS1 expression suggests that UCH37-mediated debranching

plays a critical role in facilitating the timely degradation of regulatory proteins with rapid turnover. This function may be particularly important in cellular processes that require tight temporal control, such as cell cycle progression and transcriptional reprogramming. MRFAP1 and MORF4L2, for example, are chromatin-associated proteins that function as scaffolds for assembling histone modification complexes and have been implicated in transcriptional silencing and genome stability. Their selective accumulation upon UCH37 inhibition supports a model in which debranching by UCH37 promotes the turnover of chromatin-modifying complexes, thereby enabling dynamic epigenetic regulation.

Future studies should focus on exploring the broader physiological roles of UCH37, particularly in cancer and neurodegenerative diseases, where proteasome dysfunction plays a key role[7,8,39,40]. Additionally, structural studies of Nb-ncS1 and UCH37 in complex with K48-linked Ub chains would provide deeper insights into the molecular mechanisms underlying its specificity and guide the development of more potent inhibitors. Finally, in vivo studies are necessary to validate the therapeutic potential of these nanobodies and their effects on disease models.

In conclusion, the development of Nb-cS1 and Nb-ncS1 represents a new avenue in our ability to selectively inhibit UCH37 and provide insights into the enzyme's role in regulating ubiquitin-mediated proteostasis. These findings offer promising opportunities for therapeutic intervention in diseases where UCH37 is dysregulated.

MATERIALS AND METHODS

Cell culture

Saccharomyces cerevisiae strain EBY100 (MATa AGA1::GAL1-AGA1::URA3 ura352 trp1 leu2delta200 his3delta200 pep4::HIS3 prbd1.6R can1 GAL) and yeast surface display vector, pCT used in yeast display were kindly provided by Dr. Sarah Moore (Smith College).

HEK293 stably expressing RPN11-His6-TEV-biotin tag-His6 (HEK293RPN11-HTBH) (Wang et al., 2007), UCH37KO HEK293RPN11-HTBH, and HEK293FT were cultured in DMEM medium (Genesee Scientific) supplemented with 10% fetal calf serum (Genesee Scientific), 100 units/ml penicillin and 100 µg/ml streptomycin at 37 ^{o}C in a humified atmosphere with 5% CO_2.

Plasmid and cloning

His8-MBP-TEV-UCH37 (Isoform 3) in the pVP16 vector was obtained from DNASU. His8-MBP-TEV-FLAG-UCH37 was cloned by inverse PCR with primers containing the FLAG tag. GST-3C-RPN13^{DEUBAD} (or RPN13 aa 253-407) was cloned from His10-RPN13 in pET19b, which was a gift from Joan Conaway & Ronald Conaway (Addgene plasmid # 19423). 1436 pcDNA Flag HA was a gift from William Sellers (Addgene plasmids #10792). Nanobodies were cloned into pET28b (Novagen) For bacterial

expression, and 1436 pcDNA3 Flag HA vector for mammalian expression. For Halo-tagged nanobodies, the Halo tag was introduced at the N-terminus for Nb-ncS1, and C-terminus of Nb-cS1. All PCR amplifications were performed with Phusion® High-Fidelity DNA polymerase (New England Biolabs). The primers used in this study were purchased from IDT DNA.

Construction of the synthetic nanobody (Nb) library

Our Nb library design is based on a published synthetic Nb library with slight modification and is displayed through the conventional aga1p-aga2p yeast surface display platform[30]. The Nb library was constructed by overlapping extension PCR of five oligonucleotides which composed the framework structure (oligonucleotides a and e) and randomized regions (oligonucleotides b, c, and d_{short}/ d_{medium}/ d_{long}, and e) of Nb. The oligonucleotides were generated by performing PCR using a set of ten primers (a1_f + a2_r, b3_f + b4_r, c5_f + c6_r, d7_f + d8_short_r, or d8_medium_r, or d8_long_r, and e9_f+e10_r (Supplementary Table 1). The resulting mixture (oligonucleotides a, b, c, d, and e) was mixed at equal ratios for the following overlapping extension PCR; among them, oligonucleotides d were further composed of d_{short}, d_{medium}, and d_{long} mixed at a ratio of 1:1:2 to introduce different lengths of CDR3. Both PCRs were performed using Phusion® high fidelity DNA polymerase (New England Biolabs). The combined Nb gene library pool was further amplified using pCT_nb_PstI_f and pCT_nb_BamHI_r (Supplementary Table 1). 10 µg of the amplified Nb gene library was transformed to the yeast cells with 2 µg of the NheI and BamHI (New England Biolabs) digested pCT plasmid through electroporation (Bio-Rad Gene Pulser Xcell). Dilutions of transformed yeast were then plated on a dropout medium without tryptophan (–Trp) as single colonies to obtain an estimate of library diversity. The diversity of the Nb library was further validated through next-generation sequencing (NGS).

Construction of the random mutagenized Nb-v1 and Nb-v2 library

The **Nb-v1** and **Nb-v2** gene was randomly mutagenized using Mutazyme II error-prone DNA polymerase (Agilent Technologies). The mutagenized gene library pool was then amplified with the same primers using Phusion ® high-fidelity DNA polymerase (New England Biolabs). To prepare electrocompetent yeast cells, a 50 ml culture of EBY100 cells was grown to OD 1.5 and treated with 25 mM DTT for 15 mins. The cells were then harvested, washed, and resuspended in 2 x 150 µl of ice-cold 10 mM Tris, pH 7.5, 270 mM sucrose, 2 mM $MgCl_2$. Cells were transformed separately using 2 µg of NheI and BamHI (New England Biolabs) of digested pCT vector and 10 µg of amplified Nb gene library pool through electroporation. The combined transformed cells were recovered in YPD media before being exchanged into SDCAA media. Recovered cells were serially diluted and plated in -Trp dropout media for 2-4 days at room temperature to estimate the size of the library.

Next generation sequencing

The sequencing library was generated through reduced cycle amplification to add Illumina adapters to the Nb in two sequential PCR. The libraries were pooled with 40% Phi-X library spike-in (Illumina) and sequenced on Illumina MiSeq using Nano v2-500 cycle kit, with 251 bp paired-end chemistry. The quality of the sequence data was checked using FastQC. For data analysis, the paired-end reads were merged using FLASH. The resulting reads were trimmed by BBDuk and translated with SeqKit. Downstream analysis was performed in R. The enrichment ratios of specific variants were calculated by dividing the normalized Nb frequencies enriched through sorting over the normalized Nb frequencies presented in the initial error-prone Nb-ncS1 library.

Protein purification

All protein purifications were performed at 4 ^{o}C. Biotin-Ubiquitin$_{1-75}$-propargylamine (Biotin-Ub-PA) was synthesized from Avi-tagged Ub$_{1-75}$-intein. Briefly, Avi-Ub1-75-intein was expressed in E. coli Rosetta (DE3) pLysS using 2xYT media. The cells were grown at 37 ^{o}C to OD 0.6 before being induced with 0.5 mM IPTG at 18 ^{o}C overnight. The cells were lysed in 20 mM sodium phosphate, pH 6.0, 500 mM NaCl, and 1 mM EDTA. The Avi-Ub$_{1-75}$-intein was loaded onto chitin resin (New England Biolabs). The immobilized protein was washed and then eluted with lysis buffer in the presence of 100 mM sodium 2-mercaptoethanesulfonate (MESNA) (Acros Organic) for 48 hrs at 4 ^{o}C to generate Avi-Ub1-75-MESNA through on-resin cleavage. The Avi-Ub1-75-MESNA (final concentration was 500 μM) was incubated in a buffered solution containing 20 mM Tris, pH 8.0, 10 mM N-hydroxysuccinimide, 5 mM propargylamine (Alfa Aesar) at 37°C for overnight to yield AviUb-PA.

Complexes of UCH37 and RPN13 or RPN13^{DEUBAD} were expressed and purified as previously described[27], but with a slight modification. Briefly, His-MBP-TEV-UCH37 and His-RPN13 or GST-3C-RPN13^{DEUBAD} constructs were expressed in BL21(DE3) pLysS E. coli cells grown at 37°C in LB media. The cells were grown at 37 ^{o}C to OD 0.8 before being induced with 0.4 mM IPTG at 20 ^{o}C. Cultures were harvested after 16 hr and frozen at – 80 °C. UCH37 and RPN13 or RPN13^{DEUBAD} cell pellets are mixed at 1:1 prior to lysis. Cell pellets were resuspended in lysis buffer (50 mM HEPES pH 7.4, 150 mM NaCl, 1 mM EDTA, and 1 mM TCEP), lysed by sonication, and clarified by centrifugation. UCH37•RPN13 and UCH37•RPN13^{DEUBAD} were purified following different chromatographic steps.

For UCH37•RPN13, clarified lysate was incubated with amylose resin for 2 hr at 4 °C, washed with lysis buffer, eluted with lysis buffer containing 10 mM maltose, but without EDTA, and then incubated overnight with TEV protease at 4°C to remove His-MBP tag. Then TEV protease-cleaved product was incubated with Ni-NTA resin for 1 hr, washed with Ni-NTA lysis and wash buffer (50 mM HEPES pH 7.4, 150 mM NaCl, 10 mM imidazole, and 0.5 mM TCEP), and eluted with the Ni-NTA elution buffer (50 mM HEPES pH 7.4, 150 mM NaCl, 300 mM imidazole, and 0.5 mM TCEP).

For UCH37•RPN13^{DEUBAD}, clarified lysate was incubated with Ni-NTA resin for 2 hr at 4°C, washed with Ni-NTA wash buffer, and eluted into Ni-NTA elution buffer, and then incubated overnight with TEV protease. The TEV protease cleaved product was then incubated with GST resin for 1 hr, washed with lysis buffer (50 mM HEPES pH 7.4, 150 mM NaCl, and 1 mM TCEP), and eluted with GST elution buffer (GST lysis buffer plus 10 mM glutathione). Eluate was incubated overnight with 3C protease at 4°C. For both UCH37•RPN13 and UCH37•RPN13^{DEUBAD}, the eluate was concentrated and separated on a Superdex 200 (GE) gel filtration column.

The His-Halo-nanobody/His-nanobody (Nb) variants were purified through immobilized metal affinity chromatography. The His-tagged Nbs were expressed in E. coli BL21 (DE3). The cells were grown at 37°C to OD ~0.6 before being induced at 20°C with 0.4 mM IPTG overnight. The harvested cells were lysed in 50 mM HEPES, pH 7.5, 300 mM NaCl, 10 mM imidazole, and 0.1% Triton X-100 and purified using Ni-NTA (GoldBio) affinity chromatography. The elution buffer was 50 mM HEPES, pH 7.5, 300 mM NaCl, 300 mM imidazole. The Nbs were further purified through size exclusion chromatography using a HiLoad Superdex 75 pg on an ÄKTA FPLC (GE Healthcare). The running buffer was 50 mM HEPES, pH 7.5, 300 mM NaCl, 0.5 mM TCEP.

E1, UBE2D3, UBE2R1, UBE2N/UBE2V2, UBC1, and UBE3C were purified as previously described with slight modification[27,41–44]. Briefly, E1, UBE2D3, UBE2R1, and UBE2N/UBE2V2 constructs were expressed in Rosetta 2(DE3)pLysS Escherichia coli cells grown at 37°C in LB media. Once cells reached an OD600 of 0.6–0.8, 400 µM Isopropyl ß-D-1-thiogalactopyranoside (IPTG) was added, and the temperature was reduced to 20°C to induce protein expression. Cells were then harvested after 16 hr and resuspended in Ni-NTA lysis buffer (50 mM Tris pH 7.5, 300 mM NaCl, 1 mM EDTA and 10 mM imidazole), lysed by sonication, and clarified by centrifugation. Clarified lysate was incubated with Ni-NTA resin for 2 hr at 4°C, washed with Ni-NTA lysis buffer, and eluted into Ni-NTA
elution buffer (Ni-NTA lysis buffer plus 300 mM imidazole).

NleL (aa 170–782) was purified as previously described[27,45], but with a slight modification. Briefly, NleL was expressed in BL21(DE3)pLysS E. coli cells grown at 37°C in LB media. Once cells reached an OD600 of 0.6, IPTG (200 µM) was added, and the temperature was reduced to 20°C to induce protein expression. Cells were then harvested after 16 hr and resuspended in GST lysis buffer (50 mM Tris pH 8.0, 200 mM NaCl, 1 mM EDTA, and 1 mM DTT), lysed by sonication, and clarified by centrifugation. Clarified lysate was then incubated with GST resin for 2 hr at 4°C, washed with GST lysis buffer, and eluted into GST elution buffer (GST lysis buffer plus 10 mM reduced glutathione). Eluate was concentrated in TEV protease buffer (50 mM Tris pH 8.0, and 0.5 mM TCEP), cleaved overnight with TEV protease, and further purified using anion exchange chromatography.

Generation of biotinylated Ub conjugated UCH37•RPN13^{DEUBAD}

To prepare biotinylated Ub conjugated to UCH37•RPN13^{DEUBAD}, the Avi-Ub-PA was biotinylated through BirA reaction before conjugated to UCH37•RPN13^{DEUBAD}. Briefly, the Avi-Ub-PA (final concentration was 40 μM) was added to a solution containing 10 mM Tris, pH 8.0, 5 mM $MgCl_2$, 2 mM ATP, 150 μM D(+) biotin (GoldBio), and 0.4 μM BirA at 37°C until the biotinylation reaction went to completion. The reaction was verified using MALDI-TOF MS. The 5 μM biotinylated Ub-PA was incubated with 2.5 μM UCH37•RPN13DEU in a buffered solution containing 50 mM HEPES, pH 7.5, 50 mM NaCl, 1 mM TCEP at room temperature for 1 hr with gentle rocking. The biotinylated ternary complex was further purified through size exclusion chromatography using a HiLoad Superdex 200 pg column.

Synthesis of defined Ub chains

Native homotypic K48 chains were synthesized as previously described[27]. Briefly, 1 mM Ub, 300 nM E1, and 5 μM UBE2R1 were mixed in Ub chain synthesis reaction buffer (10 mM ATP, 10 mM $MgCl_2$, 40 mM Tris-HCl pH 7.5, 50 mM NaCl, and 0.6 mM DTT) overnight at 37°C. Native K6/48 branched trimer was synthesized by mixing 2 mM K6/48R Ub, 1 mM UbD77, 300 nM E1, 5 μM UBE2D3, and 1 μM NleL in ubiquitin chain synthesis reaction buffer overnight at 37°C. Native K48/K63 branched trimer was made by first synthesizing K48 dimer by mixing 1 mM K48/K63R Ub, 1 mM UbD77, 300 nM E1, 5 μM UBE2R1, then the purified K48 dimer is mixed with 1 mM K48/K63R Ub, 300 nM E1, 3 μM UBE2N/UBE2V2 to synthesize K48/K63 branched trimer. All reactions for native chains were quenched by lowering the pH with the addition of ammonium acetate solution (pH 4.4). Enzymes were then precipitated through multiple freeze-thaw cycles and further purified using cation exchange chromatography.

Generation of high molecular weight Ub chains

Native K6/K48 and K48/K63 HMW Ub chains were synthesized as previously described[27]. Briefly, K6/K48 Ub chains were synthesized by mixing 1 mM Ub, 200 nM E1, 5 μM UBE2D3, and 1 μM NleL in Ub chain synthesis reaction buffer and K48/K63 Ub chains were synthesized using 1 mM Ub, 150 nM E1, 10 μM UBE2R1, and 5 μM UBE2N/UBE2V2 in Ub chain synthesis reaction buffer. Reaction mixtures were all incubated at 37°C overnight. All Ub chains were purified using size exclusion chromatography (Superdex 75pg) to isolate HMW chains > 75 kDa.

Selection of nanobodies against UCH37

The display of the Nb on the yeast surface was induced by resuspending 10x diversity of the Nb library in the SGCAA media at 20 ^{o}C. The induced cells were resuspended in PBSF buffer (0.1% (v/v) BSA in PBS buffer, pH 7.4) and subjected to two subsequent magnetic activated cell sorting (MACS) and two fluorescent activated cell sorting (FACS) to select Nbs to bind to Ub-UCH37•RPN13^{DEUBAD} (for Nb-ncS1 selection) or Nb-ncS1•UCH37•RPN13^{DEUBAD} (for Nb-ncS1 selection).

For MACS, the induced cells were negatively sorted against DynabeadsTM M-280

Streptavidin (ThermoFisher Scientific) before positively sorted against Dynabeads coated with biotinylated antigens in a tube setting with magnets. All MACS were performed at 4 ^{o}C for 2 hrs. For FACS, the induced cells were labeled with chicken anti-c-Myc (Exalpha biologicals INC) at 1:250 dilution for 1 hr at room temperature. The labeled cells were then incubated with varied concentrations of biotinylated antigens for 1 hr at room temperature before being simultaneously labeled with goat anti-chicken IgY (H+L) secondary antibody, Alexa FluorTM 647 and streptavidin Alexa Fluor 488 conjugate (ThermoFisher Scientific) at 1:100 dilution for 30 mins on ice in dark. Sortings were performed on a BD FACS ARIA II with 488 nm (530/30 band pass collection filter) and 640 nm (670/30 band pass filter) excitation lasers. At the end of FACS, yeast display plasmids were isolated from the enriched clones using the Zymoprep yeast plasmid miniprep kit (Zymo Research). The enriched clones were identified through random Sanger sequencing, which identified Nb-v1 (Nb-ncS1) or Nbv2 (Nb-cS1) as the most enriched clones.

Selection of nanobodies against proteasome-associated UCH37(Nb-ncS1)

The Nb-v1 library generated by error-prone PCR was cultured, induced, and washed as described above. The induced yeast cells were first labeled with chicken anti-c-Myc at 1:250 dilution for 30 mins at room temperature. This was followed by the incubation of the cells with clarified cell lysate of the HEK293RPN11-HTBH in a buffered solution containing 50 mM HEPES, pH 7.5, 50 mM NaCl, 5 mM $MgCl_2$, 2 mM ATP, 10% glycerol for 45 minutes at room temperature. The cells were then similarly labeled with the secondary antibodies and sorted through FACS as mentioned above. For negative sorting, the cell lysate of UCH37 KO HEK293TRPN11-HTBH was used as the antigen. The plasmids containing the gene of the enriched clones were extracted through the Zymoprep yeast plasmid miniprep kit and submitted for Sanger sequencing or used in the preparation of the NGS sequencing library.

Competitive sorting of nanobodies against UCH37•RPN13^{DEUBAD} and Ub-UCH37•RPN13^{DEUBAD} (Nb-cS1)

The Nbv2 library generated by error-prone PCR was cultured, induced, and washed as described above. The induced yeast cells were incubated with both FLAG-tagged UCH37•RPN13^{DEUBAD} and biotinylated Ub-UCH37•RPN13^{DEUBAD} for 1 hr at room temperature. After washing, the cells are then incubated with rabbit anti-FLAG antibody (Cell Signaling Technology) for 30 mins at room temperature. This was followed by the incubation with Alexa Fluor 647-conjugated AffiniPure Goat Anti-Rabbit IgG (Jackson ImmunoResearch) and streptavidin Alexa Fluor 488 conjugate for 30 mins on ice in the dark. The cells were then sorted through FACS selecting positive 647 and negative 488 signal clones.

In vitro pull-down assay

Halo-tagged nanobodies were immobilized on the pre-equilibrated HaloLink (Promega) resin for 2 hours at 4 ^{o}C with gentle rocking. After washing, the resin with immobilized

nanobodies was incubated with the recombinantly expressed UCH37 RPN13^{DEUBAD}, or also with Ub-UCH37•RPN13^{DEUBAD} for 2 hr at 4 ^{o}C with gentle rocking. The enriched proteins were extensively washed and eluted using 6x Laemmli loading buffer at 95°C for 3 mins before being subjected to SDS-PAGE and Western Blot analysis.

His-tagged nanobodies were immobilized on the pre-equilibrated Nickel-NTA resin (Genscript) for 2 hours at 4 ^{o}C with gentle rocking. After washing, the resin with immobilized nanobodies was incubated with the recombinantly expressed UCH37 WT or mutants in complex with RPN13^{DEUBAD} for 2 hours at 4 ^{o}C with gentle rocking. The enriched proteins were extensively washed and eluted using 6x Laemmli loading buffer at 95°C for 3 mins before being subjected to SDS-PAGE and Western Blot analysis. GST-tagged RPN13^{DEUBAD} in complex with UCH37 WT or UCH37 F117A/F121A were immobilized on the pre-equilibrated glutathione resin(Genscript) for 2 hours at 4 ^{o}C with gentle rocking. After washing, the resin with immobilized UCH37•RPN13^{DEUBAD} was incubated with 5 μM Nb-ncS1 or Nb-cS1. 5 uM homotypic K48 Ub3 or K6/48 branched Ub3 were also added in the ubiquitin chain competition pull-down. The enriched proteins were extensively washed and eluted using 6x Laemmli loading buffer at 95°C for 3 mins before being subjected to SDS-PAGE and Western Blot analysis.

Western blot analysis was imaged with Odyssey CLx Imager (LI-COR Biosciences) and performed using the following antibodies: rabbit anti-UCH37 (abcam, EPR4896), rabbit anti-Flag (Cell Signaling Technology, 14793S), rabbit anti-His tag (Cell Signaling Technology, 2365S). IRDye® 680RD goat anti-rabbit and IRDye® 800CW goat anti-mouse (LI-COR Biosciences) were used as the secondary antibodies.

Microscale thermophoresis (MST)

MST was performed to study Nb-ncS1 or Nb-cS1 with UCH37•RPN13 interaction using Monolith NT.115 Microscale Thermophoresis instrument (Nano Temper Technologies, Germany). In brief, Nb-ncS1 or Nb-cS1 was labeled with Fluorescein-isothiocyanate (Sigma) according to the manufacturer's instructions. Labeling reagents were removed by desalting column and buffer was exchanged into 50 mM Tris pH 7.4, 150 mM NaCl, and 10 mM $MgCl_2$ with 0.05% tween-20. UCH37•RPN13 were serially diluted in the same buffer, to obtain varying concentrations from 4 μM to 0.12 nM (for Nb-ncS1) or 46 μM to 2.8 nM (for Nb-cS1) and Nbs were added with a final concentration of 20 nM (Nb-ncS1) or 50 nM (Nb-cS1). The binding study was carried out using NT.115 premium capillaries, and the assay was performed in duplicates. The data for MST were recorded at room temperature at 40% LED power and IR-laser power at 40%. Data analysis was performed using MO analysis software (Nano Temper). The Kd fit model is based on a molecular interaction with a 1:1 stoichiometry according to the law of mass action.

Surface plasmon resonance (SPR)
The surface plasmon resonance experiments were performed using a BIACORE T200 (GE Healthcare) equipped with a Series S Sensor Chip NTA. The surfaces of the flow cells were conditioned using 350 mM EDTA for 1 min at a flow rate of 10 µl/min before injecting 0.5 mM $NiSO_4$ for 1 min at 10 µl/min. The purified His-Nb (15 kDa) was then injected for 2 mins at 10 µl/min and immobilized on the Ni-NTA surface at a density of approximately 30 response units (RU). Single cycle kinetic titration experiments were performed by injecting purified UCH37 at increasing concentrations in 50 mM HEPES, pH 7.5, 50 mM NaCl, 50 µM EDTA, 0.005% (w/v) TWEEN 20 at a flow rate of 30 µl/min with a 300 s contact time and 900 s dissociation time. The flow cell surfaces were regenerated using 2 pulses of 350 mM EDTA for 2 min at a flow rate of 10 µl/min. The sensorgrams were double-referenced before analyzed using BIAevaluation (GE Healthcare). The association and dissociation rate constant, ka and kd, were determined from the direct curve fitting to a 1:1 binding model; the dissociation equilibrium constant, K_D, was calculated from k_{off}/k_{on}. All experiments were performed at 25 ^{o}C.

Size exclusion chromatograph-multi angle light scattering (SEC-MALS) analysis
SEC-MALS was performed in a TSKgel G3000SWXL column (TOSOH Biosciences) on a Agilent 1260 Infinity HPLC system (Agilent Technologies) coupled to a MALS detector, DAWN HELEOS II (Wyatt Technology) and a refractive index detector, Optilab T-rEX (Wyatt Technology). Nanobodies were incubated with UCH37•RPN13^{DEUBAD} on ice for 30 mins before the analysis. The flow rate was 1.0 ml/min and the mobile phase was 50 mM sodium phosphate, pH 6.5, 150 mM sodium chloride, and 10% isopropanol. Data was analyzed using Astra (Wyatt Technology) and the molar masses of the complexes were determined by the Zimm fit model. All the experiments were performed at room temperature.

HDX-MS analysis
Sample preparation. To assess the deuterium uptake difference between free UCH37•RPN13^{DEUBAD} and Nb bound UCH37•RPN13^{DEUBAD}, UCH37•RPN13^{DEUBAD} (45 µM) were pre-incubated with the Nb (90 µM) for 1 hr on ice in dilution buffer (50 mM HEPES, pH 7.4, 50 mM NaCl, and 0.5 mM TCEP). To assess the uptake differences between free Nb and UCH37•RPN13^{DEUBAD} bound Nb, UCH37•RPN13^{DEUBAD} (45 uM) were pre-incubated with Nb (45 uM) to avoid the presence of unbound Nb. All further steps, including deuterium labeling and reaction quench were performed on Trajan's LEAP HDX platform (Trajan Scientific and Medical, Ringwood, Victoria, Australia). 4 µL of protein complex was diluted into either 96 µL of H_2O buffer (20 mM sodium phosphate, pH 7.0 in H_2O) for reference mapping or 96 µL of D_2O buffer (20 mM sodium phosphate, pD 7.0 in D_2O, 99.9% D_2O from Cambridge Isotopes) to initiate deuterium labeling. After different times of exposure to the deuterated buffer at 15°C, 50 µL labeling reaction was quenched by mixing with 50 µL quenching buffer (0.8 M Guanidine-HCl, 1% acetic acid, pH 2.2) at 4°C. 50 uL of quenched samples were

immediately injected into the LC-MS platform.

HDX-MS data acquisition. The LC-MS data acquisition was performed on the ACQUITY UPLC M-Class System (Waters Corp.) and Synapt G2Si HDMS (Waters Corp.). Before the experiment, the MS instrument was calibrated in the positive ion mode using sodium iodide. The data was acquired in the positive mode in the mass range 100-2000 m/z using ESI with the following parameters: capillary voltage 2.5 kV, sampling cone 40 V, source offset 30 V, source temperature 80°C, desolvation temperature 175°C, cone gas 90 L/h, desolvation gas flow 600 L/h, nebulizer pressure 5 bar. To minimize hydrogen gas phase back exchange and keep the optimal separation of peptides within ion mobility cell, ion optics parameters were adjusted (StepWave transfer offset 15 V, DA1 3 V, DA2 0 V; IMS wave velocity 700 m/s, IMS wave height 40 V). Upon injection, samples were passed through an immobilized pepsin column (Enzymate BEH Pepsin Column, 2.1 × 30 mm, Waters Corp.) at 100 µL/min for inline digestion at 10°C. Following digestion, the resulting peptides were desalted on a ACQUITY UPLC HSS T3 VanGuard Pre-column (C18, 1.8 µm, 100 A, 2.1 × 5 mm, Waters Corp.) and separated on a ACQUITY UPLC HSS T3 microbore column (C18, 1.8 µm, 100 A, 1.0 × 50 mm, Waters Corp.) at 0°C with linear gradient of 80% B (A is 0.1% formic acid [FA] in H_2O, and B is 0.1% FA in acetonitrile) over 12 min. The identification of peptides was performed using the data from the undeuterated sample acquired in MS^e mode, while HDX data was acquired using HDMS in resolution mode.

HDX data analysis. Peptide identification was conducted using Protein Lynx Global Server (PLGS) version 3.0.1 software (Waters Corp). Data acquired from undeuterated samples were searched against the sequence database of proteins present in the complexes. Processing parameters include 556.2771 Da/e as lock mass for charge +1, lock mass window of 0.25 Da, and non-specific primary digest reagent. Data from peptides generated from PLGS were imported into DynamX 3.0 (Waters Corp.) to determine the deuterium uptake of samples. The following PLGS filtering parameters were applied: peptide quality thresholds of MS1 signal intensity greater than 5000, minimum products per amino acid of 0.3, maximum mass error of 1 ppm, retention time RSD of 0.5%, and PLGS score greater than 7. Following the automated peptide search and ion detection, each spectrum was manually inspected to ensure the corresponding m/z and isotopic distributions at various charge states were properly assigned to the appropriate peptic peptide. The uptake for all time points were averaged between three replicates. The percent relative deuterium uptake was calculated by dividing the relative deuterium uptake of each peptic peptide by its theoretical maximum uptake. Statistical significance for the differential HDX data is determined by t-test for each time point, and a 95% confidence limit for the uncertainty of the mean relative deuterium uptake was calculated to determine the threshold for significant uptake difference.

Native mass spectrometry

Native MS analysis was performed after buffer exchanging proteins into the 150 mM

ammonium acetate (AmAc) solution pH 6.8 using Amicon Ultra-0.5 Centrifugal Filter Units (Millipore Sigma). For the stoichiometry analysis of the UCH37•RPN13^{DEUBAD} and Nb-ncS1 complex, UCH37•RPN13^{DEUBAD} variants were premixed with Nb-ncS1 in the equimolar ratio and the solution was incubated on ice for 1 hour. For the analysis of Nb-ncS1 bound to UCH37•RPN13^{DEUBAD} -Ub-PA, the reaction between UCH37•RPN13^{DEUBAD} and Ub-PA was performed for 1 hour at 37°C prior mixing with Nb-ncS1. The samples were further diluted using 150 mM AmAc pH 6.8 to the final 10 uM concentration for the MS analysis. All native MS measurements were performed on a Synapt G2 HDMS (Waters Corp.) hybrid quadrupole/time-of-flight mass spectrometer equipped with a nanospray ion source. The following set of parameters was used: capillary voltage, 1.2 kV; sampling cone voltage, 40 V; extraction cone voltage 4 V. To enhance the transmission of the high-MW complexes, the backing pressure was increased up to 4 mBar. The MS data were analyzed with MassLynx 4.2 software (Waters Corp.); deconvolution of the mass spectra and calculation of the complex intact mass were performed using a UniDEC algorithm.

AlphaFold 3 Modeling

Structural models of protein complexes were generated using AlphaFold 3 via the Google AlphaFold Server (https://deepmind.google/discover/alphafold), using the default multimer modeling settings. Amino acid sequences for UCH37, Ub, RPN13, and Nb-ncS1 were provided as input, reflecting the stoichiometry observed in the experimental system. No structural templates or experimental constraints were applied. Five models were generated per prediction, each revealing a similar, high-confidence inter-chain predicted TM (ipTM) score for the UCH37-Nb-ncS1 interface. Model confidence was assessed using ipTM and Predicted Aligned Error (PAE) plots. Figures were rendered in ChimeraX (v1.7) using the final AlphaFold 3 model.

Protein crystallization and data processing

Individually purified UCH37 WT, RPN13 269-388, and cNb protein were incubated in a 1:2:2 ratio on ice for 4 hrs and subject to size exclusion chromatography using a HiLoad Superdex75 column (Cytiva) with 50 mM Tris pH 7.4, 100 mM NaCl, and 1 mM DTT as the mobile phase. Fractions of interest consisting of all three components of the complex were determined by SDS-PAGE Coomassie staining, pooled and concentrated to 25 mg/mL. The UCH37 WT, RPN13 269-388 and cNb complex was crystallized by sitting drop vapor diffusion at 21°C first identified in the commercial PEG Ion HT Screen (Hampton Research). Crystals grown in 0.1 M Sodium citrate tribasic dihydrate pH 5.6, 2% v/v Tacsimate pH 5.0, 16% w/v Polyethylene glycol 3,350 diffracted to 2.4 Å at the Advanced Photon Source (APS) at Argonne National Laboratory on the GM/CA 23-ID-B beamline. Data was processed using HKL3000 in the orthorhombic space group $C222_1$.

Structure determination and refinement

The structure of the UCH37 WT, RPN13 269-388, and Nb-cS1 complex was

determined by molecular replacement using the program PHASER in the Phenix Suite. Input models used for molecular replacement were the heterodimer complex of UCH37 with RPN13 DEUBAD previously solved by Sixma and colleagues (PDB 4UEM) in addition to a homology model of the cNb generated by SWISS-MODEL with the primary sequence of the cNb and tertiary structure of the camelid Lag30 nanobody bound to eGFP (PDB 7SAI).

Model building and refinement was carried out using COOT and phenix refine where the current crystallographic R and R_{free} are 0.235 and 0.271 respectively. Analysis of the Ramachandran plot indicated that 94.9% of residues fall within the most favored regions, 5.1% of residues fall within the allowed region, and none were observed in the disallowed region. Within the structure solution 65 of water molecules and 4 chloride ions are observed. While electron density is well resolved for structured regions, specific portions of the structure lacks depiction of a large number of residues. UCH37 WT is well resolved in regions 5-59, 74-149, 161-247, 253-312. All other regions, which includes about 55 residues, were not well resolved in the density. RPN13 269-388 was not well resolved in 31 residues which included residues 269-286, 357-359, and 385-388. The Nb-cS1 was not well resolved at positions 1-22, 48, 49, and 137. The final structure of the heterotrimer complex was validated using MolProbity and deposited in the Protein Data Bank under the accession code 9E7K.

Ub-AMC assays

Ub-AMC assays were performed in black-well, 384-well plates (Corning). Mixtures containing UCH37•RPN13 (2 nM) with or without various concentrations of nanobodies in assay buffer (50 mM HEPES pH7.4, 50 mM NaCl, 0.5 mM TCEP) were incubated at 37°C for 15 min. 500 nM final concentration of Ub-AMC was then added to the appropriate wells, and hydrolysis was monitored continuously for 30 min at 37°C on a fluorescence plate reader (BioTek Synergy 2, λex = 360 nm, λem = 460 nm).

Ub-Propargylamine (Ub-PA) labeling assay

2.5 μM of UCH37•RPN13 and indicated concentrations of Nb-cS1 or Nb-ncS1 in assay buffer (50 mM HEPES pH 7.4, 50 mM NaCl, 0.5 mM TCEP) were incubated at 37°C for 15 min. Ub-PA (2.5 μM) was then added and the reaction was incubated at 37°C for 30 min. Reactions were quenched by the addition of 6x Laemmli loading buffer. Samples were separated on a 15% SDS-PAGE gel and transferred on a PVDF membrane, stained with Streptavidin Alexa Fluor 647 (Thermo Fisher S32357) and imaged on the Odyssey CLx Imager (LI-COR Biosciences).

Ub chain debranching assay

The debranching assays were performed as previously described (Deol et al., 2020), but with slight modifications. For the debranching assays, recombinant 1 μM UCH37•RPN13 with or without various concentrations of nanobodies were warmed to

37°C in DUB buffer for 15 minutes. Then 0.2 mg/ml HMW Ub chains or 10 μM branched Ub3 were added. Reactions were incubated for 1 hr at 37 °C and then quenched with 6x Laemmli loading buffer. Samples were separated on a 15% SDS-PAGE gel and either stained with SYPRO Ruby total protein stain or transferred on a PVDF membrane and blotted with mouse anti-ubiquitin antibody (Enzo Life Sciences, BML-PW0930-0100).

Ub middle-down mass spectrometry (Ub MiD MS) analysis

K6/K48 HMW Ub chains treated with UCH37•RPN13 and nanobodies were quenched by freeze and thaw cycles. Lbpro* at final concentration of 15 μM was then added and incubated overnight to induce cleavage after R74 position of Ub[46]. The reaction was then quenched with 10% acetic acid (v/v) to precipitate other proteins except ubiquitin. The supernatant contains ubiquitin is dialyzed to water and reconstitute in 50% acetonitrile (v/v), and 0.1% formic acid (v/v). Samples were injected at a flow rate of 10 μl/min and ionized using a heated electrospray ionization (HESI-II) source before being analyzed using the Orbitrap Fusion Tribid mass spectrometer (Thermo Scientific). The resolving power of the mass analyzer on the spectrometer was set at 120000. All spectra were processed with in-house software (MASH Suite) using a signal-to-noise (S/N) threshold of 3 and a fit factor of 70% and then validated manually (Guner et al., 2014). Percentages correspond to the relative quantification values of the 11+ charge state for all three species: Ub1-74, 1xdiGly-Ub1-74, and 2xdiGly-Ub1-74.

Kinetic analysis of Nb-ncS1 inhibition

Stock solutions of UCH37•RPN13, K6/K48Ub chains, and Nb-ncS1 were prepared in DUB buffer (50 mM HEPES pH 7.5, 50 mM NaCl, and 1 mM DTT).UCH37•RPN13 was kept constant at 0.5 μM with varied concentrations of K6/K48Ub chains and Nb-ncS1 as described in the figure. All reactions were performed at 37°C. Each sample along with a Ub and di-Ub standard was then separated on a 15% SDS-PAGE gel and stained with SYPRO Ruby. Gels were visualized on a Typhoon FLA 9500 (GE), and densitometry was performed using Image Studio. Initial velocities of Ub and di-Ub formation were converted to concentration per minute (μM/min). These values were then fit to the Michealis-Menten equation using nonlinear regression with competitive inhibition equation. Two biological replicates for each reaction were performed.

Proximity ligation assay (PLA)

HEK293FT or HEK293FT UCH37KO cells were transfected with nanobodies as described above. 48 hr after transfection, cells were fixed with 4% paraformaldehyde and permeablized with 0.1% triton in PBS. The cells are then blocked with 3% BSA and incubated with rabbit anti-UCH37(Thermo Fisher, PA5-110544) or rabbit anti-UCHL3(Proteintech, 12384-1-AP) and mouse anti-HA (Cell Signaling Technology, 2367S) primary antibodies at 4 °C overnight. For PLA assay, the cells were incubated with Duolink In Situ PLA Probe Anti-Mouse MINUS and Anti-Rabbit PLUS, followed by

ligation and amplification with Duolink In Situ Detection Reagents Red, and stained with DAPI. Cells were imaged with a Nikon TiE stand A1 Resonant Scanning Confocal microscope.

Immunoprecipitation for western blotting

10 cm^2 dishes of HEK293FT cells were grown and transfected with FLAG-tagged Nb in the 1436 pCDNA3 Flag HA vector (a gift from William Sellers, Addgene plasmids #10792). Transient transfections were performed using Xfect transfection reagent (Takara Bio) according to the manufacturer's protocol. The harvested cells were lysed in 50 mM HEPES, pH 7.5, 50 mM NaCl, 5 mM $MgCl_2$, 2 mM ATP, 1 mM DTT, and 10% glycerol before being incubated with anti-FLAG resin (Genscript) for 3 hours at 4 ^oC. The immunoprecipitated proteins were washed extensively with 50 mM HEPES, pH 7.5, 150 mM NaCl, 5 mM $MgCl_2$, 2 mM ATP, 1 mM DTT, 0.05% IGEPAL prior to elution using 6x Laemmli loading buffer at 95 ^oC for 3 mins. Western blot analysis was performed using the following antibodies: rabbit anti-UCH37 (abcam, EPR4896), rabbit anti-ADRM1 (Cell Signaling Technology, D9Z1U), rabbit anti-PSMD14 (abcam, EPR4258), rabbit anti-PSMC1 (abcam, ab3317), mouse anti-PSMA2 (Cell Signaling Technology, 11864S) and rabbit anti-Flag (Cell Signaling Technology, 14793S) at 1:1000 dilution. IRDye® 680RD goat anti-rabbit and IRDye® 800CW goat anti-mouse (LI-COR Biosciences) were used as the secondary antibodies at 1:15000 dilution.

Immunoprecipitation for mass-spectrometry

15 cm^2 dishes of HEK293FT cells were grown and transfected with HaloTag nanobodies as described above. The harvested cells were lysed and immunoprecipitated similarly as described above. The immunoprecipitated proteins were washed extensively with 50 mM HEPES, pH 7.5, 150 mM NaCl, 5 mM $MgCl_2$, 2 mM ATP, and 1 mM DTT. The bound proteins were reduced with 10 mM DTT at 37 ^oC for 1 hr and alkylated using 25 mM iodoacetamide (Sigma-Aldrich) in 25 mM NH_4CO_3 at room temperature for 1 hr in the dark before being subjected to on-bead trypsin digestion using sequencing grade modified trypsin (Promega) for overnight at 37 ^oC. Tryptic digests were desalted with Sep-Pak C18 cartridge (Waters), quantified by Pierce Quantitative Colorimetric Peptide Assay, and then subjected to TMT labeling. 10 µL of each sample (20-40 µg) peptides in 100 mM TEAB were added with 5 µL of 20 ng/µL 10-plex TMT reagents (Thermo Scientific) dissolved in anhydrous acetonitrile. Following incubation at RT for 1 hr, the labeling reaction was quenched with hydroxylamine to a final concentration of 0.4 % (v/v) for 15 min, and the equal volume of TMT labeled samples were pooled together. Peptides were desalted with Sep-Pak C18 cartridge (Waters) and separated by a homemade fused silica capillary column (75 µm x 150 mm) packed with C-18 resin (120A, 1.9 µm, Dr. Maisch HPLC GmbH) with the EASY-nLC 1000 nano-HPLC system (ThermoFisher Scientific), which was coupled with the Orbitrap Fusion Tribrid mass spectrometer. The scan sequence began with an MS1 spectrum (Orbitrap analysis; resolution 120,000; mass range 375–1500 m/z; automatic gain control [AGC] target 5×10^5; maximum injection time 50ms).

MS2 analysis consisted of CID with 35% energy (AGC 5 × 10^3; isolation window 1.2 Th; maximum injection time 50 ms; activation time 10 ms). Monoisotopic peak assignment was used, and previously interrogated precursors were excluded using a dynamic window (15 s ± 10 ppm), and dependent scans were performed on a single charge state per precursor. Following the acquisition of each MS2 spectrum, a synchronous-precursor-selection (SPS) MS3 scan was collected on the top 10 most intense ions in the MS2 spectrum. MS3 precursors were fragmented by high energy CID with 65% energy and analyzed using the Orbitrap (AGC 5 × 10^4 maximum injection time 86 ms, resolution was 50,000 at 2 Th isolation window).

Global proteomics of Nb-ncS1 transfected cells

HEK293FT cells plated in a six-well plate were grown and transfected with Halo-tagged Nb-ncS1 as described above. For the bortezomib-treated samples, bortezomib was added at 1 μM for 8 hr prior to harvesting. Three biological replicates were done for each condition. All samples were treated with 250 μM H_2O_2 for 2 hr prior to harvesting. Cells were then suspended in lysis buffer (8 M urea, 50 mM HEPES pH 7.4, 75 mM NaCl, and 1× protease inhibitor cocktail) and lysed by freeze-thaw cycles and sonication. Clarified lysates of 100 μg protein was then reduced with 5 mM TCEP for 30 minutes and then alkylated with 20 mM iodoacetamide in the dark for 1 hr at room temperature. Proteins are precipitated by cold acetone overnight, and then resuspended in 100 mM TEAB buffer and digested by trypsin overnight at 37°C. The peptides are quantified by Pierce Quantitative Colorimetric Peptide Assay and then subjected to TMT labeling.

5 μL of 20 ng/μL 10-plex TMT reagents (Thermo Scientific) dissolved in anhydrous acetonitrile were added to 20 μg of digested peptide samples. Following incubation at RT for 1 hr, the labeling reaction was quenched with hydroxylamine to a final concentration of 0.4 % (v/v) for 15 min, and the equal volume of TMT labeled samples were pooled together. Pooled peptides were dried using a vacuum centrifuge and fractionated into 8 samples by Pierce™ High pH Reversed-Phase Peptide Fractionation Kit. Peptides were then separated on a 75 μm × 50 cm, nanoViper C18, 2 μm, 100 Å column (ThermoFisher Scientific) with the EASY-nLC nano-HPLC system (ThermoFisher Scientific), which was coupled with the Orbitrap Fusion Tribrid mass spectrometer. The gradient is 5% (0–10 min), 5–35% (10–150 min), 35–85% (150–160 min) in solvent B (0.1% FA in acetonitrile) in solvent A (0.1% FA in H_2O) over a total 200 min run at 300 nL/min

The scan sequence began with an MS1 spectrum (Orbitrap analysis; resolution 120,000; mass range 375–1500 m/z; automatic gain control [AGC] target 5 × 10^5; maximum injection time 50ms). MS2 analysis consisted of CID with 35% energy (AGC 5 × 10^3; isolation window 1.2 Th; maximum injection time 50 ms; activation time 10 ms). Monoisotopic peak assignment was used, and previously interrogated precursors were excluded using a dynamic window (15 s ± 10 ppm), and dependent scans were performed on a single charge state per precursor. Following acquisition of each MS2

spectrum, a synchronous-precursor-selection (SPS) MS3 scan was collected on the top 10 most intense ions in the MS2 spectrum. MS3 precursors were fragmented by high energy CID with 65% energy and analyzed using the Orbitrap (AGC 5×10^4 maximum injection time 86 ms, resolution was 50,000 at 2 Th isolation window).

The raw files generated were processed with Proteome Discoverer 2.5 (Thermo Fisher Scientific) and the search engine SEQUEST HT. Processing workflow for SPS MS3 reporter ion-based quantification was used, with MS2 (CID) for peptide identification and MS3 (HCD) to acquire TMT reporter ions for quantification. The spectrum was searched against the UniProt human (Homo sapiens) database (Dec 14, 2022 released). The following search settings were applied: trypsin digestion with up to two missed cleavages, a peptide mass tolerance of 10 ppm, a fragment mass tolerance of 0.6 Da, carbamidomethylation of cysteine (+57.021 Da), and TMT 6-plex N-terminal/lysine residues (+229.163 Da) were included as static modifications, Methionine oxidation (+15.995 Da) and N-Terminal acetylation (+42.011 Da) were included as dynamic modifications. The resulting peptide hits were filtered for a maximum of 1% FDR using the Percolator algorithm.

Western blot analysis of MRFAP1 and MORF4L2

HEK293FT or UCH37KO HEK293FT cells were grown and transfected with Halo-tagged Nb-ncS1 as described above. Cells were treated with 250 μM H_2O_2 for 2 hr, harvested and lysed with RIPA buffer for western blot analysis.

For the emetine chase experiment, the cells are not harvested but changed with media containing 50 μM emetine, with or without 1 μM bortezomib, and incubated for 8 hr. The cells are then harvested and lysed with RIPA buffer for western blot analysis.

For the UCH37 knock-down experiment with siRNA, 6 nM of three different UCH37 siRNAs or one negative control siRNA (pre-designed siRNA from IDT) were transfected in MDA-MB-231 cells and Hela cells using Lipofectamine® RNAiMAX transfection reagent (Life Technologies). After 48 h, the cells were harvested and lysed with RIPA buffer for western blot analysis.

Western blot analysis was imaged with Odyssey CLx Imager (LI-COR Biosciences) and performed using the following antibodies: rabbit anti-MRFAP1 (Proteintech, 11639-1-AP) and rabbit anti-MORF4L2 (Proteintech, 14710-1-AP). IRDye® 680RD goat anti-rabbit and IRDye® 800CW goat anti-mouse (LI-COR Biosciences) were used as the secondary antibodies.

DATA AVAILABILITY

The structural coordinates for Nb-cS1 in complex with UCH37•RPN13^{DEUBAD} have been deposited in RCSB Protein Data Bank (PDB) under accession code 9E7K.

Source data are provided within this paper (Source data.zip). Additional data can be obtained from the corresponding author upon request.

INCLUSION & ETHICS STATEMENT

All collaborators who meet the authorship criteria required by Nature Portfolio journals have been included as authors, as their contributions were essential to the design and execution of the study. This research was conducted without any restrictions or prohibitions on the researchers and does not pose risks of stigmatization, incrimination, discrimination, or personal harm to the participants.

MATERIALS & CORRESPONDENCE

Correspondence to Eric R. Strieter

CONFLICT OF INTEREST

Eric R. Strieter: ERS declares outside interest in Relay Therapeutics. The other authors declare that no competing interests exist.

ACKNOWLEDGEMENTS

We thank Dr. Steve Eyles (UMass Amherst) for assistance with high-resolution MS at UMass Amherst Mass Spectrometry Core Facility (RRID:SCR_019063), Dr. Amy S. Burnside (UMass Amherst) for assistance with flow cytometry, and Dr. Ravi Ranjan for the NGS experiment at the UMass Amherst Genomics Resource Laboratory. MST, SPR and SEC-MALS data were acquired in the UMass Amherst Biophysical Characterization Core Facility (RRID:SCR_022357). The PLA data was gathered at the UMass Amherst Light Microscopy Facility. This work was funded by the National Institutes of Health (NIH) (R35GM149532 to E.R.S. and R01GM126296 to C.D.), an NIH Chemistry and Biology Training Grant (T32GM139789 to J.D.), and an NIH Ruth L. Kirschstein NRSA (F31CA275390 to R.P.). The data described herein were acquired on an Orbitrap Fusion mass spectrometer funded by NIH grant 1S10OD010645-01A1.

AUTHOR CONTRIBUTIONS

ERS: Conceived the project, conceptualization, funding acquisition, supervision, and data analysis. YL, LHC, ES and JD: Generated and characterized the nanobodies. RP and CD: Solved and analyzed the crystal structure. YL, ES and ERS wrote the manuscript.

REFERENCES

1. Oh, E., Akopian, D. & Rape, M. Principles of Ubiquitin-dependent signaling. *Annu. Rev. Cell. Dev. Biol.* **34**, 137–162 (2018).
2. Randles, L., Anchoori, R. K., Roden, R. B. S. & Walters, K. J. The Proteasome Ubiquitin Receptor hRpn13 and Its Interacting Deubiquitinating Enzyme Uch37 Are Required for Proper Cell Cycle Progression. *J. Biol. Chem.* **291**, 8773–8783 (2016)

3. Mazumdar, T. *et al.* Regulation of NF-κB activity and inducible nitric oxide synthase by regulatory particle non-ATPase subunit 13 (Rpn13). *Proc. Natl. Acad. Sci.* **107**, 13854–13859 (2010).
4. Nishi, R. *et al.* Systematic characterization of deubiquitylating enzymes for roles in maintaining genome integrity. *Nat. Cell. Biol.* **16**, 1016–1026 (2014).
5. Lim, J. H. *et al.* CYLD negatively regulates transforming growth factor-β-signalling via deubiquitinating Akt. *Nat. Commun.* **3,** 771 (2012).
6. Imai, Y., Soda, M. & Takahashi, R. Parkin Suppresses Unfolded Protein Stress-induced Cell Death through Its E3 Ubiquitin-protein Ligase Activity. *J. Biol. Chem.* **275**, 35661–35664 (2000).
7. McKinnon, C. *et al.* Early-onset impairment of the ubiquitin-proteasome system in dopaminergic neurons caused by α-synuclein. *Acta. Neuropathol. Commun.* **8**, 17 (2020).
8. Nalepa, G., Rolfe, M. & Harper, J. W. Drug discovery in the ubiquitin–proteasome system. *Nat. Rev. Drug. Discov.* **5**, 596–613 (2006).
9. Popovic, D., Vucic, D. & Dikic, I. Ubiquitination in disease pathogenesis and treatment. *Nat. Med.* **20**, 1242–1253 (2014).
10. Fraile, J. M., Quesada, V., Rodríguez, D., Freije, J. M. P. & López-Otín, C. Deubiquitinases in cancer: new functions and therapeutic options. *Oncogene* **31**, 2373–2388 (2011).
11. Harrigan, J. A., Jacq, X., Martin, N. M. & Jackson, S. P. Deubiquitylating enzymes and drug discovery: emerging opportunities. *Nat. Rev. Drug. Discov.* **17**, 57–78 (2017).
12. Hamazaki, J. *et al.* A novel proteasome interacting protein recruits the deubiquitinating enzyme UCH37 to 26S proteasomes. *EMBO. J.* **25**, 4524–4536 (2006).
13. Jørgensen, J. P. *et al.* Adrm1, a Putative Cell Adhesion Regulating Protein, is a Novel Proteasome-associated Factor. *J. Mol. Biol.* **360**, 1043–1052 (2006).
14. Qiu, X.-B. *et al.* hRpn13/ADRM1/GP110 is a novel proteasome subunit that binds the deubiquitinating enzyme, UCH37. *EMBO. J.* **25**, 5742–5753 (2006).
15. Yao, T. *et al.* Proteasome recruitment and activation of the Uch37 deubiquitinating enzyme by Adrm1. *Nat. Cell. Biol.* **8**, 994–1002 (2006).
16. Yao, T. *et al*. Distinct modes of regulation of the UCH37 deubiquitinating enzyme in the proteasome and in the INO80 Chromatin-Remodeling complex. *Mol. Cell.* **31**, 909–917 (2008).
17. Chen, Y. *et al.* Expression and clinical significance of UCH37 in human esophageal squamous cell carcinoma. *Dig. Dis. Sci.* **57**, 2310–2317 (2012).
18. Wang, L. *et al*. High expression of UCH37 is significantly associated with poor prognosis in human epithelial ovarian cancer. *Tumor. Biol.* **35**, 11427–11433 (2014).
19. Han, W. *et al.* Ubiquitin C-terminal hydrolase37 regulates Tcf7 DNA binding for the activation of Wnt signalling. *Sci. Rep.* **7**, 42590 (2017).
20. Arpalahti, L. *et al*. UCHL5 expression associates with improved survival in lymph-node-positive rectal cancer. *Tumor. Biol.* **39**, 101042831771607 (2017).

21. Arpalahti, L. *et al*. Positive cytoplasmic UCHL5 tumor expression in gastric cancer is linked to improved prognosis. *PLoS ONE* **13**, e0193125 (2018).
22. D'Arcy, P. *et al*. Inhibition of proteasome deubiquitinating activity as a new cancer therapy. *Nat. Med.* **17**, 1636–1640 (2011).
23. Wang, X. *et al*. The proteasome deubiquitinase inhibitor VLX1570 shows selectivity for ubiquitin-specific protease-14 and induces apoptosis of multiple myeloma cells. *Sci. Rep.* **6**, 26979 (2016).
24. Tian, Z. *et al*. A novel small molecule inhibitor of deubiquitylating enzyme USP14 and UCHL5 induces apoptosis in multiple myeloma and overcomes bortezomib resistance. *Blood* **123**, 706–716 (2013).
25. Gubat, J. *et al*. Comprehensive target screening and cellular profiling of the Cancer-Active compound B-AP15 indicate abrogation of protein homeostasis and organelle dysfunction as the primary mechanism of action. *Front. Oncol.* **12**, (2022).
26. Ward, J. *et al*. Re-Evaluating the Mechanism of Action of α,β-Unsaturated Carbonyl DUB Inhibitors b-AP15 and VLX1570: A Paradigmatic Example of Unspecific Protein Cross-linking with Michael Acceptor Motif-Containing Drugs. *J. Med. Chem.* **63**, 3756–3762 (2020).
27. Deol, K. K. *et al.* Proteasome-Bound UCH37/UCHL5 debranches ubiquitin chains to promote degradation. *Mol. Cell.* **80**, 796-809.e9 (2020).
28. Song, A. *et al.* Branched ubiquitin chain binding and deubiquitination by UCH37 facilitate proteasome clearance of stress-induced inclusions. *eLife* **10**, e72798 (2021).
29. Du, J. *et al.* A cryptic K48 ubiquitin chain binding site on UCH37 is required for its role in proteasomal degradation. *eLife* **11**, (2022).
30. McMahon, C. *et al.* Yeast surface display platform for rapid discovery of conformationally selective nanobodies. *Nat. Struct. Mol. Biol.* **25**, 289–296 (2018).
31. Ekkebus, R. *et al.* On Terminal Alkynes That Can React with Active-Site Cysteine Nucleophiles in Proteases. *J. Am. Chem. Soc.* **135**, 2867–2870 (2013).
32. Sahtoe, D. D. *et al.* Mechanism of UCH-L5 Activation and Inhibition by DEUBAD Domains in RPN13 and INO80G. *Mol. Cell.* **57**, 887–900, (2015).
33. VanderLinden, R. T. *et al.* Structural Basis for the Activation and Inhibition of the UCH37 Deubiquitylase. *Mol. Cell.* **57**, 901–911, (2015).
34. Abramson, J. *et al.* Accurate structure prediction of biomolecular interactions with AlphaFold 3. *Nature* **630**, 493–500 (2024).
35. Gullberg, M. *et al.* Cytokine detection by antibody-based proximity ligation. *Proc. Natl. Acad. Sci.* **101**, 8420–8424 (2004).
36. Harris, I. S. *et al.* Deubiquitinases Maintain Protein Homeostasis and Survival of Cancer Cells upon Glutathione Depletion. *Cell. Metab.* **29**, 1166-1181.e6 (2019).
37. Li, J. *et al.* Proteome-wide mapping of short-lived proteins in human cells. *Mol. Cell.* **81**, 4722-4735.e5 (2021).
38. Mevissen, T. E. T. & Komander, D. Mechanisms of Deubiquitinase Specificity and Regulation. *Annu. Rev. Biochem.* **86**, 159–192 (2017).
39. Manasanch, E. E. & Orlowski, R. Z. Proteasome inhibitors in cancer therapy. *Nat. Rev. Clin. Oncol.* **14**, 1649–1657 (2017).

40. Ciechanover, A. & Brundin, P. The ubiquitin proteasome system in neurodegenerative diseases: Sometimes the chicken, sometimes the egg. *Neuron* **40**, 427-446 (2003).
41. Bashore, C. *et al.* Ubp6 deubiquitinase controls conformational dynamics and substrate degradation of the 26S proteasome. *Nat. Struct. Mol. Biol.* **22**, 712–719, (2015).
42. Michel, M. A. *et al.* Assembly and specific recognition of K29- and K33-linked polyubiquitin. *Mol. Cell.* **58**, 95–109 (2015).
43. Pham, G. H. *et al.* Comparison of native and non-native ubiquitin oligomers reveals analogous structures and reactivities. *Protein Sci.* **25**, 456–471 (2016).
44. Trang, V. H. *et al.* Nonenzymatic polymerization of ubiquitin: Single-step synthesis and isolation of discrete ubiquitin oligomers. *Angew. Chem. Int. Ed.* **51**, 13085–13088 (2012).
45. Valkevich, E. M., Sanchez, N. A., Ge, Y. & Strieter, E. R. Middle-Down mass spectrometry enables characterization of branched ubiquitin chains. *Biochemistry* **53**, 4979–4989 (2014).
46. Swatek, K. N. *et al.* Insights into ubiquitin chain architecture using Ub-clipping. *Nature* **572**, 533–537 (2019).

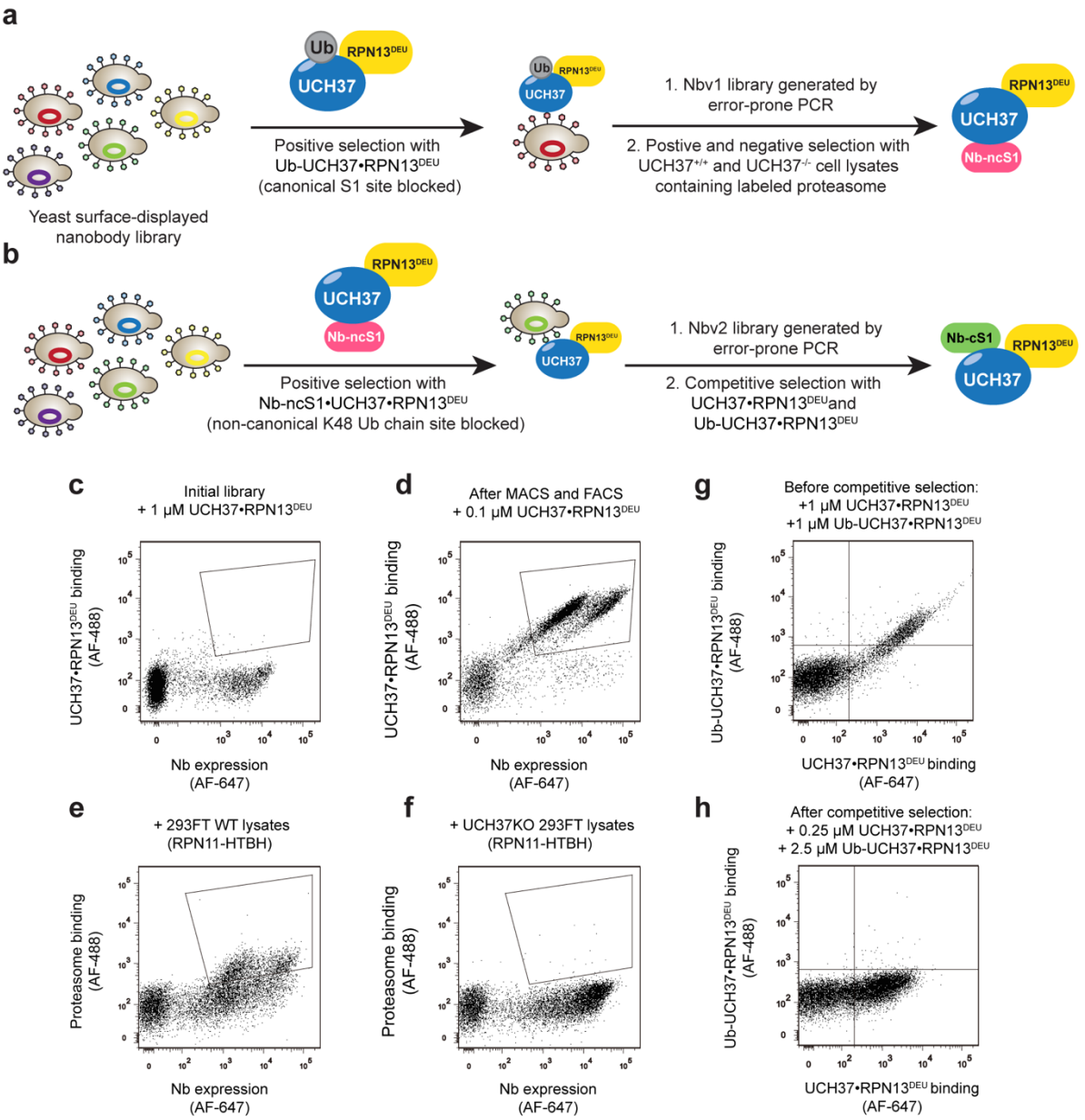

Figure 1: Screening strategy for the isolation of UCH37 nanobodies

(a) General scheme of Nb-ncS1 identification. Nb variants that bind to Ub-UCH37•RPN13^{DEUBAD} were enriched after several rounds of MACS and FACS, which include Nb-v1 as the most frequent clone. Nb-v1 was then diversified with error-prone PCR to generate a library for additional screening with HEK293FT or UCH37KO HEK293FT lysates containing biotinylated proteasomes.

(b) General scheme of Nb-cS1 identification. Nb variants that bind to Nb-ncS1•UCH37•RPN13^{DEUBAD} were enriched after several rounds of MACS and FACS, which include Nbv2 as the most frequent clone. Nbv2 was then diversified with error-prone PCR to generate a library for additional screening with Flag-tagged UCH37•RPN13^{DEUBAD} (cS1 site free) and biotinylated Ub-UCH37•RPN13^{DEUBAD} (cS1 site blocked by Ub).

(c-d) Scatter plots of initial library (c) and after MACS and FACS with biotinylated Ub-

UCH37•RPN13^{DEUBAD} (d). Clones with high Nb expression and strong binding were enriched.

(e-f) Scatter plots after positive and negative sorting against HEK293FT and UCH37KO HEK293FT lysates containing biotinylated proteasomes (RPN11-HTBH). Clones were enriched with high Nb expression and strong binding to WT proteasome (e) but not to UCH37KO proteasome (f).

(g-h) Scatter plots before competitive sorting against Flag-tagged UCH37•RPN13^{DEUBAD} and biotinylated Ub-UCH37•RPN13^{DEUBAD}. A large population of Nbs binds to both targets ((g), positive signal along the x-axis and y-axis). After competitive sorting, clones showed selective binding toward UCH37•RPN13^{DEUBAD} ((h), positive signal along x-axis, negative signal along y-axis).

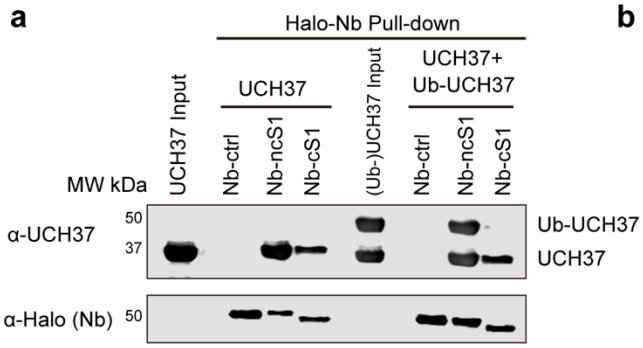

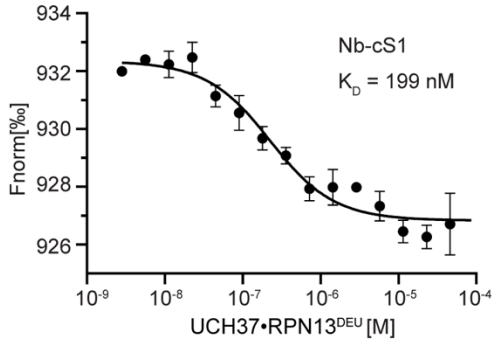

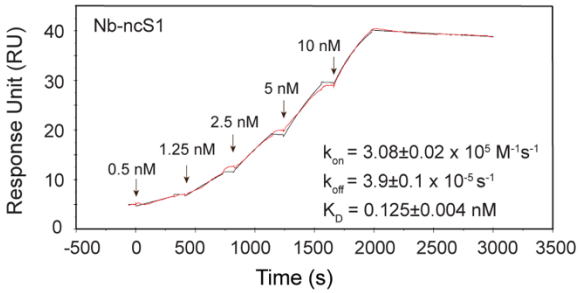

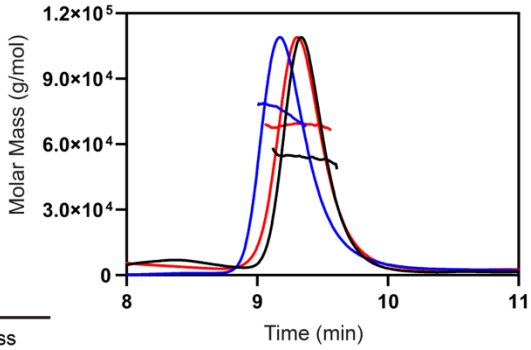

e

Protein	Molar Mass Measured (kg/mol)	Molar Mass Theoretical (kg/mol)
UCH37•RPN13^{DEU}	54.1 ± 1.3	52.6
UCH37•RPN13^{DEU}•Nb-ncS1	75.0 ± 2.1	68.1
UCH37•RPN13^{DEU}•Nb-cS1	68.8 ± 1.0	67.4

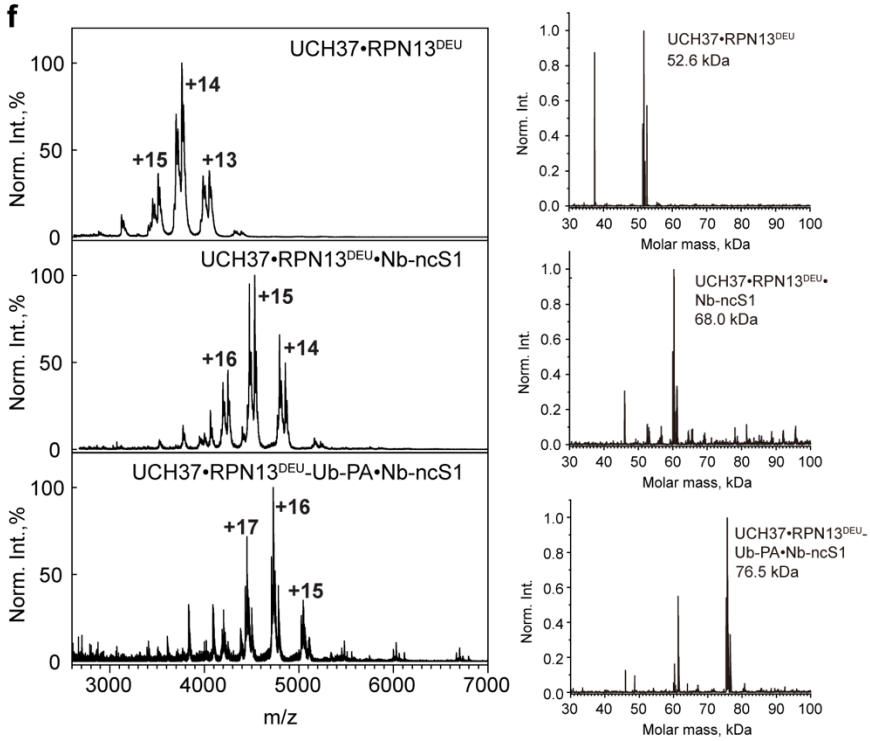

Figure 2: Nb-ncS1 and Nb-cS1 Bind to UCH37 with High Affinities

(a) Western blot analysis of Halo-tagged nanobody pull-downs with UCH37•RPN13^{DEUBAD} or a mixture of UCH37•RPN13^{DEUBAD} and Ub-UCH37•RPN13^{DEUBAD}. Nb-ncS1 pulls down UCH37•RPN13^{DEUBAD} whether it's conjugated to Ub or not, while Nb-cS1 can only pull down UCH37•RPN13^{DEUBAD}. Immunoblotting was performed with the α-UCH37 antibody and α-Halo tag antibody.

(b) Microscale thermophoresis (MST) experiments showing affinity between Nb-cS1 and UCH37•RPN13, n = 2 independent measurements, error bars represent the standard deviation.

(c) Single-cycle surface plasmon resonance (SPR) experiment showing the interaction between Nb-ncS1 and UCH37. Experimental data is in red, and the curve fit is in black.

(d) SEC-MALS elution profile of UCH37•RPN13^{DEUBAD}(black) or UCH37•RPN13^{DEUBAD} incubated with Nb-ncS1(blue) or Nb-cS1(red).

(e) Theoretical and measured molar mass of UCH37•RPN13^{DEUBAD} and its complex with Nb-ncS1 or Nb-cS1 obtained from SEC-MALS measurements.

(f) Native ESI-MS spectra of free UCH37•RPN13^{DEUBAD} (top panel), Nb-ncS1-bound UCH37•RPN13^{DEUBAD} (middle panel), and Nb-ncS1 bound to Ub-UCH37•RPN13^{DEUBAD} (bottom panel). Additional peaks observed in the +13 to +15 charge states for free UCH37 •RPN13^{DEUBAD} and in the +14 to +16 charge states for the complex correspond to N-/C-terminal truncations in the DEUBAD domain of RPN13. Deconvoluted spectra corresponding to each raw trace are shown to the right.

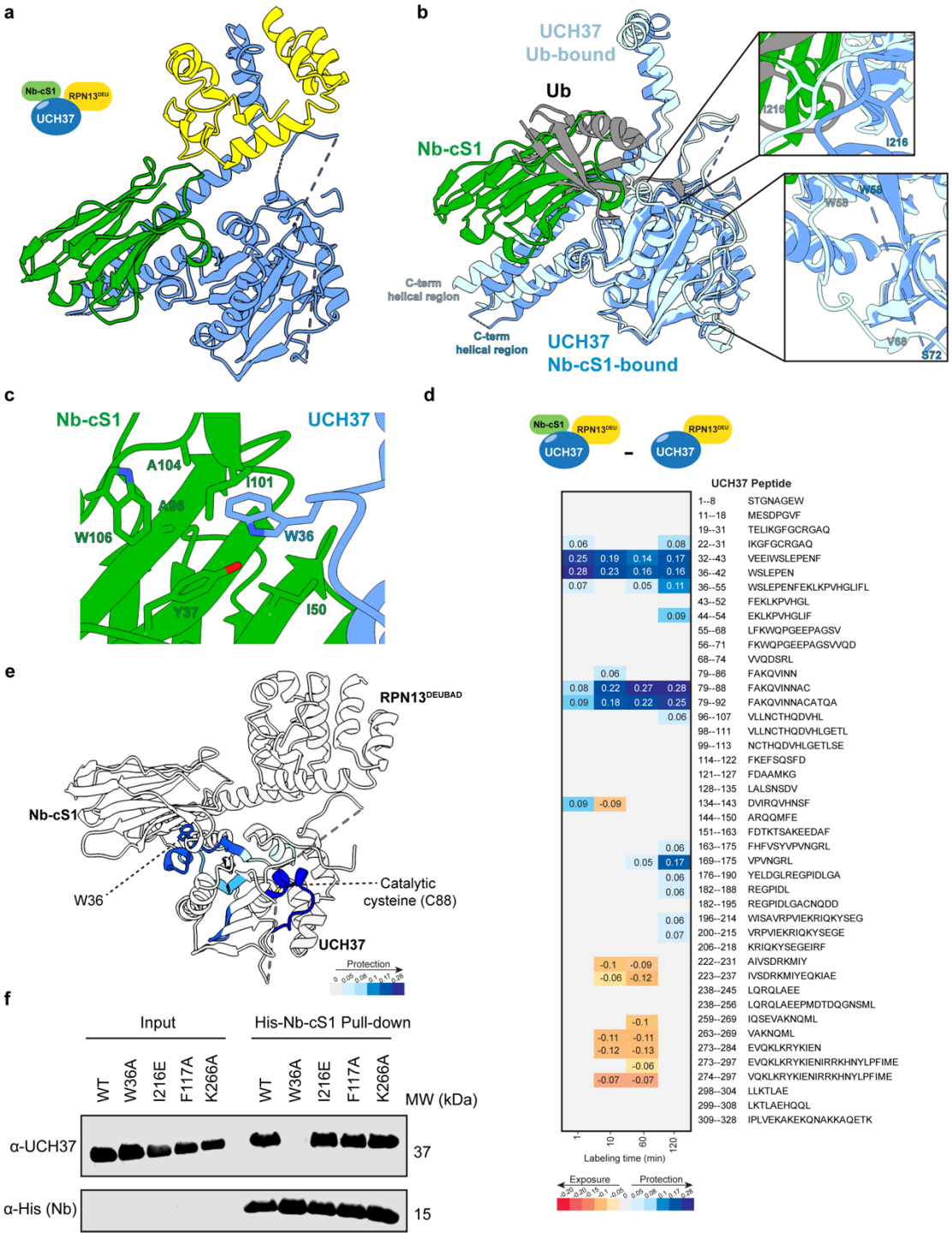

Figure 3: Structure of Nb-cS1 bound to UCH37•RPN13^{DEUBAD}

(a) X-ray structure of Nb-cS1 (green) bound to UCH37 (blue) in complex with RPN13^{DEUBAD} (yellow).

(b) Overlay of Nb-cS1-bound and Ub-bound (PDB: 4uel) structures with RPN13^{DEUBAD} omitted for clarity. Highlighted are the differences in the C-terminal helical regions of UCH37, as well as the loop containing I216 and residues 60–71.

(c) Interaction of UCH37 W36 (blue) with a pocket in Nb-cS1 consisting of largely hydrophobic residues (green).

(d) Differential deuterium uptake plot comparing UCH37•RPN13^{DEUBAD} in the presence and absence of Nb-cS1. Each data point represents the difference in deuterium uptake between the Nb-cS1-bound and free forms of the complex at the indicated time point.

(e) Structure of UCH37•RPN13^{DEUBAD} bound to Nb-cS1 showing regions with statistically significant differences in deuterium exchange upon noncovalent binding of Nb-cS1. The data correspond to 2 h of deuterium labeling.

(f) Western blot analysis of 6xHis-tagged Nb-cS1 pull-downs with UCH37•RPN13^{DEUBAD} variants. UCH37 W36A reduces binding to Nb-cS1. UCH37 I216E reduces binding of Ub to the canonical Ub-binding site[32]. UCH37 F117A reduces binding of K48-linked Ub chains to the noncanonical Ub-binding site[29]. UCH37 K266A is a substitution located in the C-terminal helical domain. Immunoblotting was performed with the α-UCH37 antibody and α-His tag antibody.

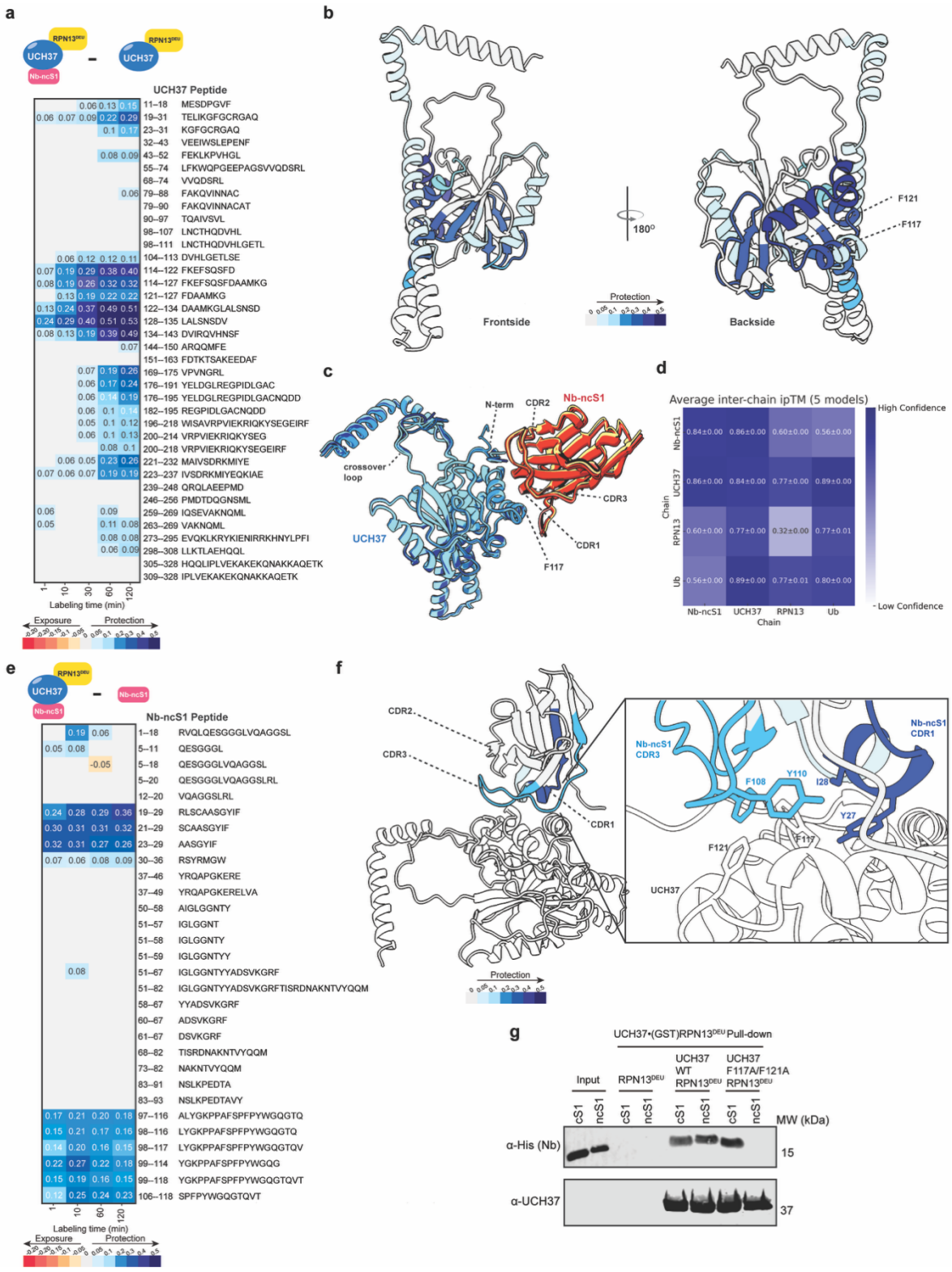

Figure 4: Nb-ncS1 is predicted to bind the aromatic-rich motif of UCH37

(a) Differential deuterium uptake plot comparing UCH37•RPN13^{DEUBAD} in the presence and absence of Nb-ncS1. Each data point represents the difference in deuterium uptake between the Nb-ncS1-bound and free forms of the complex at the indicated time point.

(b) AlphaFold 3 model of UCH37 showing regions with statistically significant differences in

deuterium exchange upon noncovalent binding of Nb-ncS1. The data correspond to 2 h of deuterium labeling.

(c) Overlay of five AlphaFold 3 models of Nb-ncS1 bound to the Ub adduct of UCH37•RPN13. For clarity, Ub and RPN13 are omitted from the visualization.

(d) Heat map showing the average inter-chain interface predicted TM-score (ipTM) across all five AlphaFold 3 models. The ipTM score for the Nb-ncS1 and UCH37 interface is 0.86, which indicates a high-confidence, high-quality prediction.

(e) Differential deuterium uptake plot comparing Nb-ncS1 in the presence and absence of UCH37•RPN13^{DEUBAD}. Each data point represents the difference in deuterium uptake between the UCH37•RPN13^{DEUBAD}-bound and free forms of the complex at the indicated time point.

(f) AlphaFold 3 model of Nb-ncS1 bound to UCH37•RPN13^{DEUBAD}, highlighting regions with statistically significant changes in deuterium exchange upon noncovalent binding. The complementarity-determining regions (CDRs) 1 and 3 of Nb-ncS1 are predicted to engage UCH37 directly, forming hydrophobic contacts with the aromatic-rich motif on the backside of UCH37.

(g) Western blot analysis of pulldowns with UCH37•(GST-tagged)RPN13^{DEUBAD} variants and either 6xHis-tagged Nb-cS1 or Nb-ncS1. UCH37 F117A/F121A reduces binding to Nb-ncS1, but not Nb-cS1. Immunoblotting was performed with the α-UCH37 antibody and α-His tag antibody.

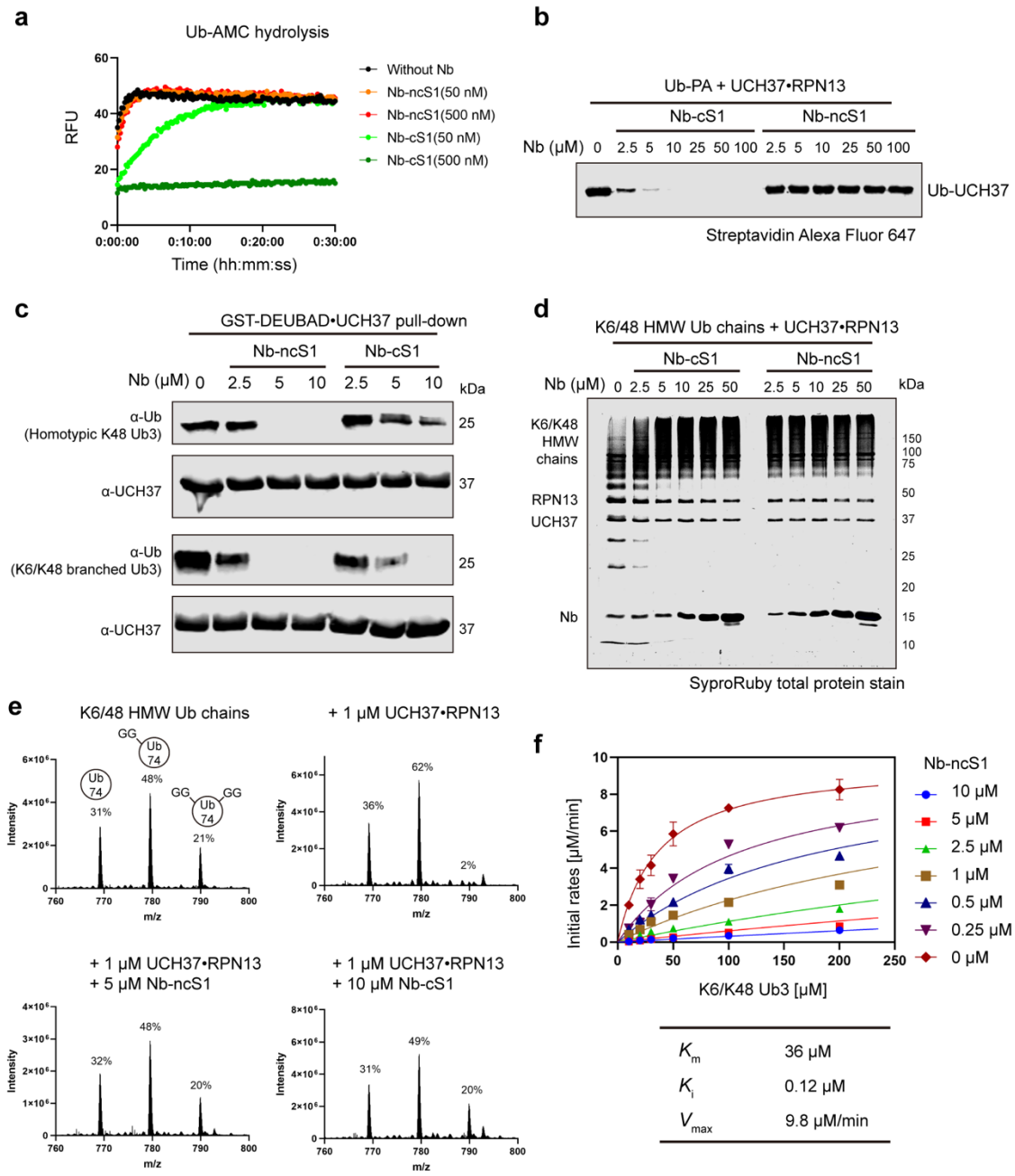

Figure 5: Nb-ncS1 and Nb-cS1 have different effects on the DUB activity of UCH37

(a) Hydrolysis of Ub-AMC (500 nM) by UCH37•RPN13^{DEUBAD} (2 nM) with the indicated concentrations of nanobodies. The released AMC fluorescence is monitored with excitation and emission wavelengths at 360 nm and 460 nm with a plate reader.

(b) Western blot analysis of biotinylated Ub-propargylamine (2.5 μM) labeling by UCH37•RPN13^{DEUBAD} (2.5 μM) with the indicated concentrations of nanobodies. Immunoblotting was performed with Alexa Fluor 647-conjugated streptavidin.

(c) Western blot analysis of UCH37•(GST-tagged)RPN13^{DEUBAD} pull-downs with homotypic K48 Ub3 or K6/K48 branched Ub3 (5 μM) with the indicated concentrations of nanobodies.

(d) SDS-PAGE analysis of the cleavage of K6/K48 high-molecular weight (HMW) Ub chains (0.2 mg/ml) with UCH37•RPN13 (1 μM) co-incubated with different concentrations of

nanobodies. Gels were imaged by SYPRO Ruby staining.

(e) Middle-down MS analysis of HMW K6/K48 chains (0.2 mg/ml) subjected to UCH37•RPN13 (1 μM) co-incubated with different concentrations of nanobodies. Percentages correspond to the relative quantification values of the 11+ charge state for each Ub species: Ub1–74, 1xdiGly-Ub1–74, and 2xdiGly-Ub1–74.

(f) Kinetic analyses of the cleavage of K6/K48 tri-Ub with UCH37•RPN13 (0.5 μM) with different concentrations of Nb-ncS1. Reactions were separated on a 15% SDS-PAGE gel and followed by SYPRO® Ruby staining. Initial velocities of Ub and di-Ub formation were converted to concentration (μM) per minute with Ub standards. These values were then fitted to the Michealis-Menten equation using nonlinear regression in Prism. Error bars represent the standard deviation of two experiments.

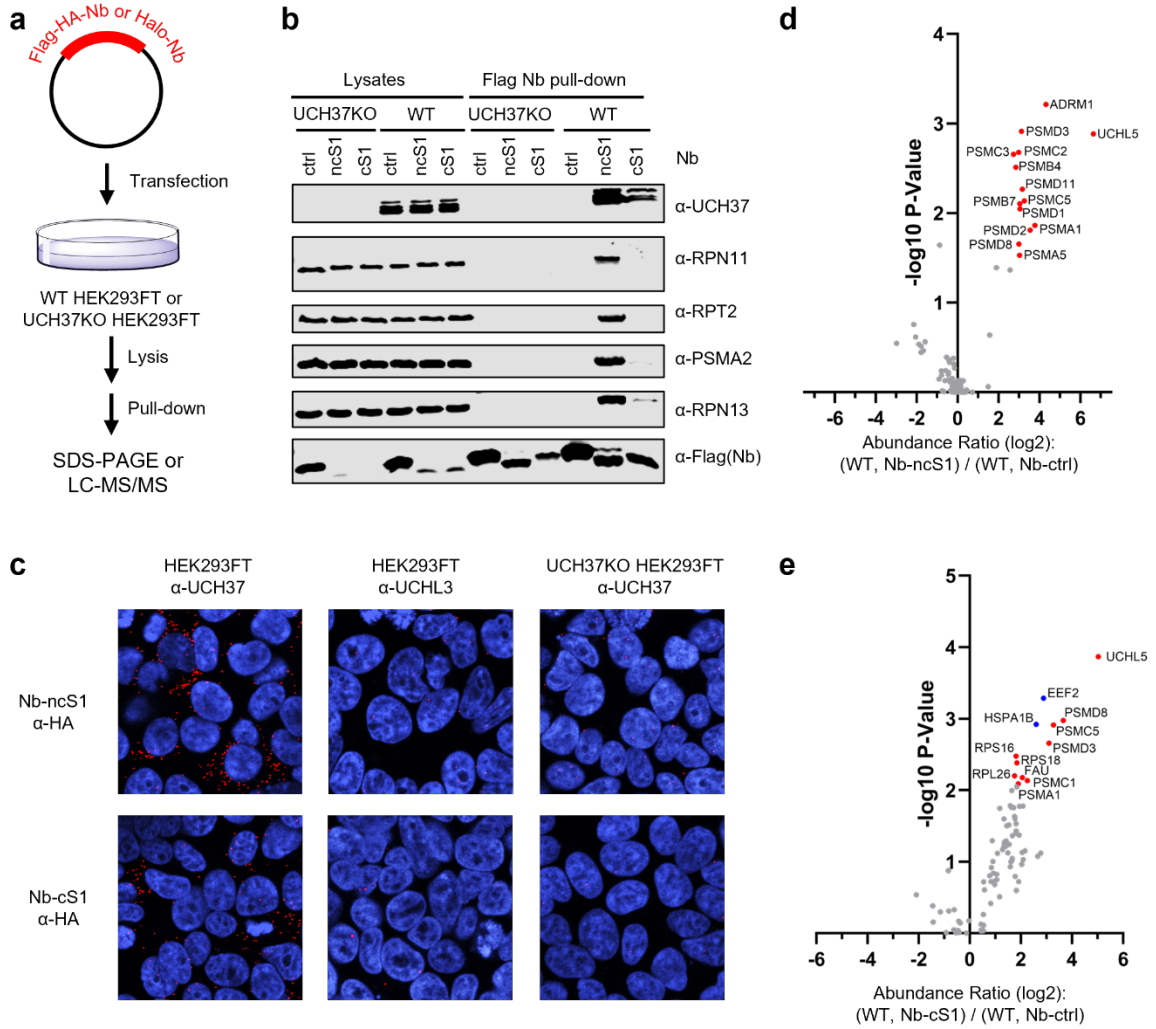

Figure 6: Nanobodies selectively interact with UCH37 in cells

(a) WT or UCH37KO HEK293FT cells were transfected with tagged nanobodies. Pulled-down proteins were analyzed by SDS-PAGE and LC-MS/MS.

(b) Western blot analysis of anti-FLAG pull-downs with HEK293FT cell lysates transfected with FLAG tagged nanobodies. Samples were separated by SDS–PAGE and immunoblotted against UCH37 along with other proteasome subunits.

(c) Proximity ligation assay (PLA) with HEK293FT cells transfected with different nanobodies. Cells were fixed and stained with the indicated antibodies followed by PLA. Blue: DAPI, RED: PLA signal.

(d) Volcano plot from IP-TMT-MS data comparing proteins enriched by Halo-tagged Nb-ncS1 versus the Halo-tagged control nanobody (Nb-ctrl). UCH37 (UCHL5) along with other proteasomal subunits are shown in red.

(e) Volcano plot from IP-TMT-MS data comparing proteins enriched by Halo-tagged Nb-cS1 versus the Halo-tagged control nanobody (Nb-ctrl). UCH37 (UCHL5) along with other proteasomal subunits and ribosomal proteins are shown in red.

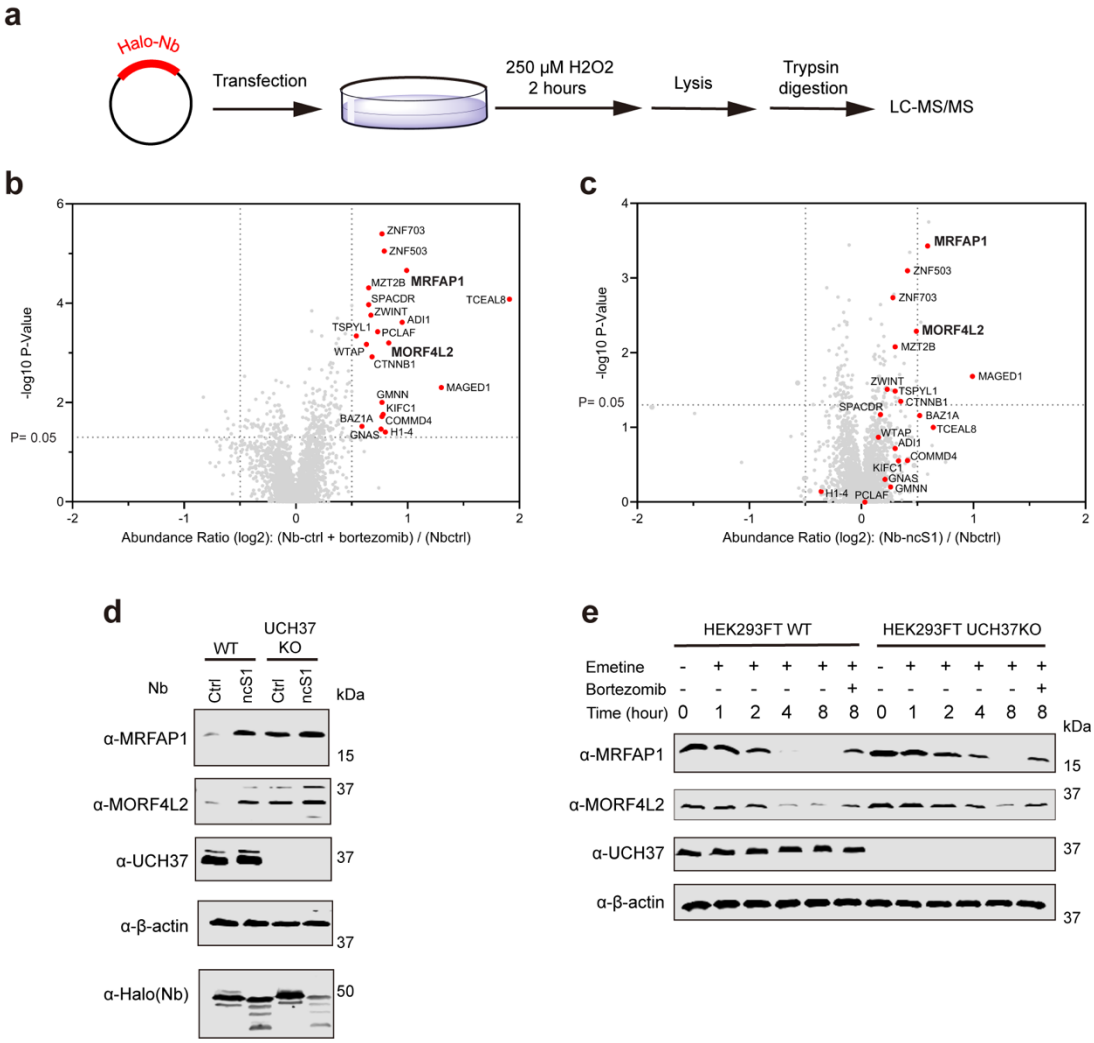

Figure 7: Nanobodies Identify Potential UCH37 Substrates

(a) HEK293FT cells were treated with H_2O_2 (250 µM) for 2 h, followed by lysis to analyze differences in protein abundance caused by the presence of either the proteasome inhibitor bortezomib or Nb-ncS1 by TMT based quantitative proteomics.

(b) Volcano plots comparing the proteomes of bortezomib+Nb-ctrl treated and Nb-ctrl only HEK293FT cells.

(c) Volcano plots comparing the proteomes of Nb-ncS1 transfected and Nb-ctrl transfected HEK293FT cells.

(d) Western blot analysis of MRFAP1 and MORF4L2 from WT and UCH37KO HEK293FT cells transfected with nanobodies.

(e) Western blot analysis of the turnover of MRFAP1 and MORF4L2 after shutting off translation with emetine in WT and UCH37KO HEK293FT cells for the indicated period of time.

SUPPLEMENTARY FIGURES

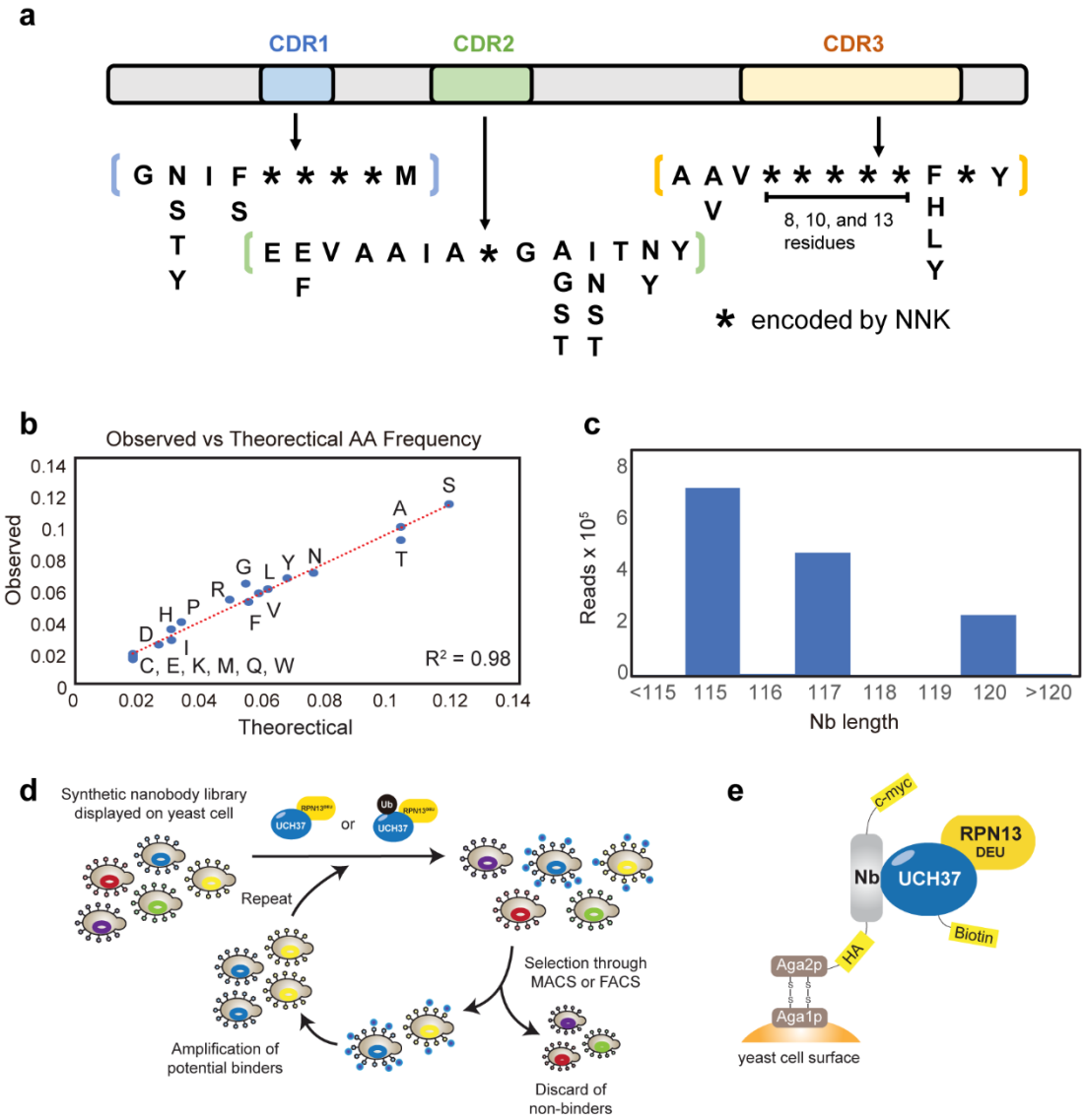

Supplementary Figure 1: Construction and NGS Analysis of the Synthetic Nanobody Library

(a) General scheme of the synthetic nanobody highlights fixed framework regions (shown in gray), while the CDR loops: CDR1 (blue), CDR2 (green), and CDR3 (orange) were designed with variations. Partial randomization in these loops was introduced by PCR using primers with different degenerate codons. Highly variable regions were introduced by PCR using primers with NNK codons, marked by asterisks (*).

(b) The amino acid frequencies at the diversified positions within the CDRs. The results demonstrated that the distribution of amino acids in the library closely aligned with the target values.

(c) Bar plot showing the distribution of the ensemble of nanobodies based on their length.

(d) General scheme of the nanobody selection process. Yeast displaying nanobodies with affinity to antigen are shown being isolated via MACS or FACS, amplified, and undergoing iterative rounds of selection

(e) General scheme of the yeast display platform. The nanobody is shown with an N-terminal HA tag and a C-terminal c-myc tag, and fused to the C-terminal of Aga2p which tethers the nanobody to the yeast cell wall.

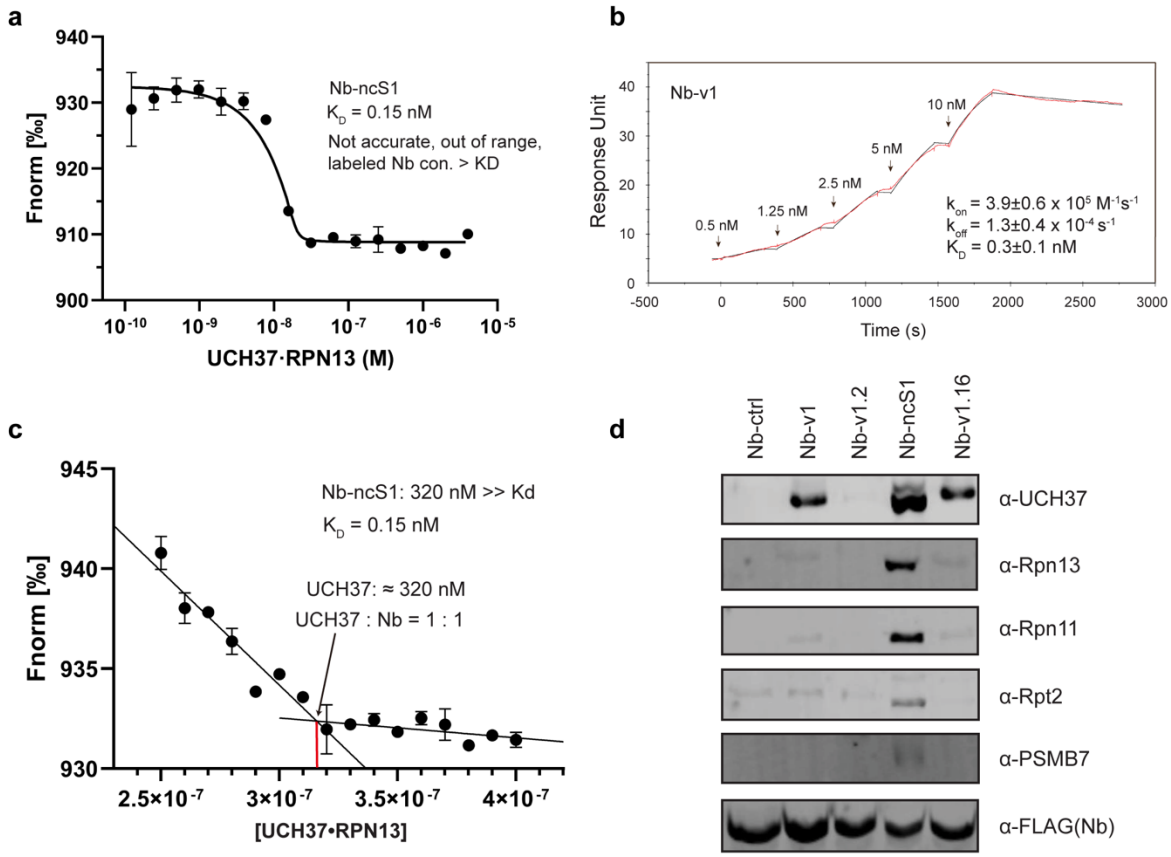

Supplementary Figure 2: Biophysical Characterization of Nb-v1 and Nb-ncS1

(a) Microscale thermophoresis (MST) experiments showing affinity between Nb-ncS1 and UCH37•RPN13.The measured K_D value (0.15 nM) is far below the concentration of the fluorescently labeled Nb-ncS1 (20 nM) and the K_D is outside the optimal range for the instrument.

(b) Single-cycle surface plasmon resonance (SPR) experiment showing the interaction between Nb-v1 and UCH37. Experimental data is in red, and the curve fit is in black.

(c) Microscale thermophoresis (MST) experiments showing stoichiometry between Nb-ncS1 and UCH37•RPN13. Fluorescently labeled Nb-ncS1 is used at a concentration much higher than Kd (320 nM vs 0.13 nM) to ensure the UCH37•RPN13 titrated in is fully occupied and produces a signal. The kink point is where all Nb-ncS1 is bound by UCH37•RPN13

(d) Western blot analysis of anti-FLAG pull-downs with HEK293FT cell lysates transfected with FLAG-Halo-tagged nanobodies. Samples were separated by SDS–PAGE and immunoblotted against UCH37 along with other proteasome subunits. Nb-v1.2 and Nb-v1.16 are two other mutants of Nb-v1.

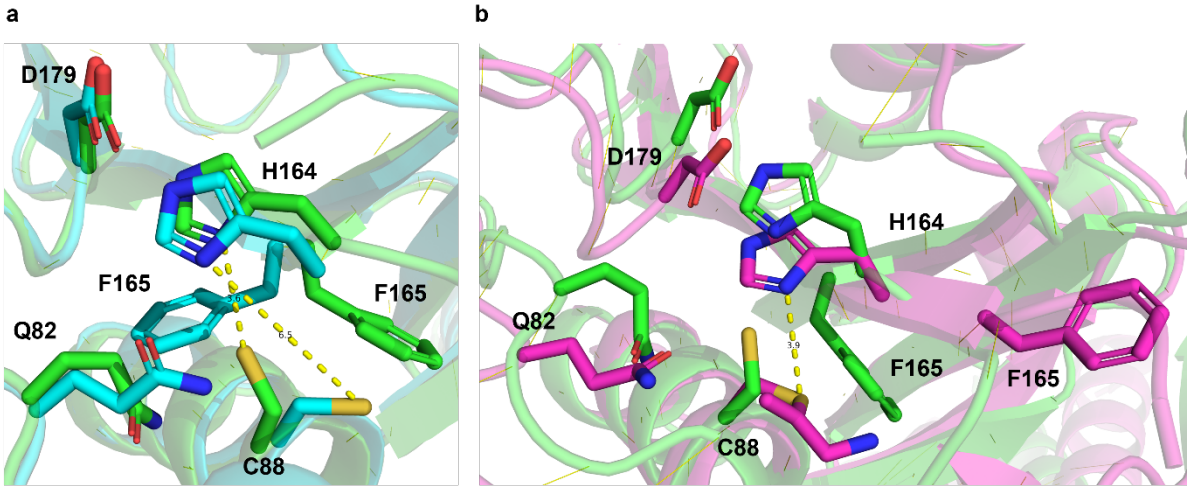

Supplementary Figure 3: Nb-cS1-Induced Conformational Change of UCH37 Active Site
Structural comparison of the Nb-cS1 with UCH37•RPN13^{DEUBAD} complex (green) with the UCH37 structures from the apo state (PDB 4UEM, cyan) and Ub-bound state (PDB 4UEL, purple), focused on the active site of UCH37. Key residues involved in the active site—D179, H164, F165, Q82, and C88—are highlighted. In the apo state (4UEM and PDB 3RII), the catalytic triad (C88, H164, D179) is misaligned. Monoubiquitin binding, as shown in the Ub-bound structure (4UEL), induces a conformational change that aligns C88 with H164, promoting a productive conformation. Our Nb-cS1-bound UCH37 structure also promotes alignment of the catalytic triad into a productive conformation while occupying the cS1 site, suggesting the mechanism of inhibition might not be dominated through active site rearrangement.

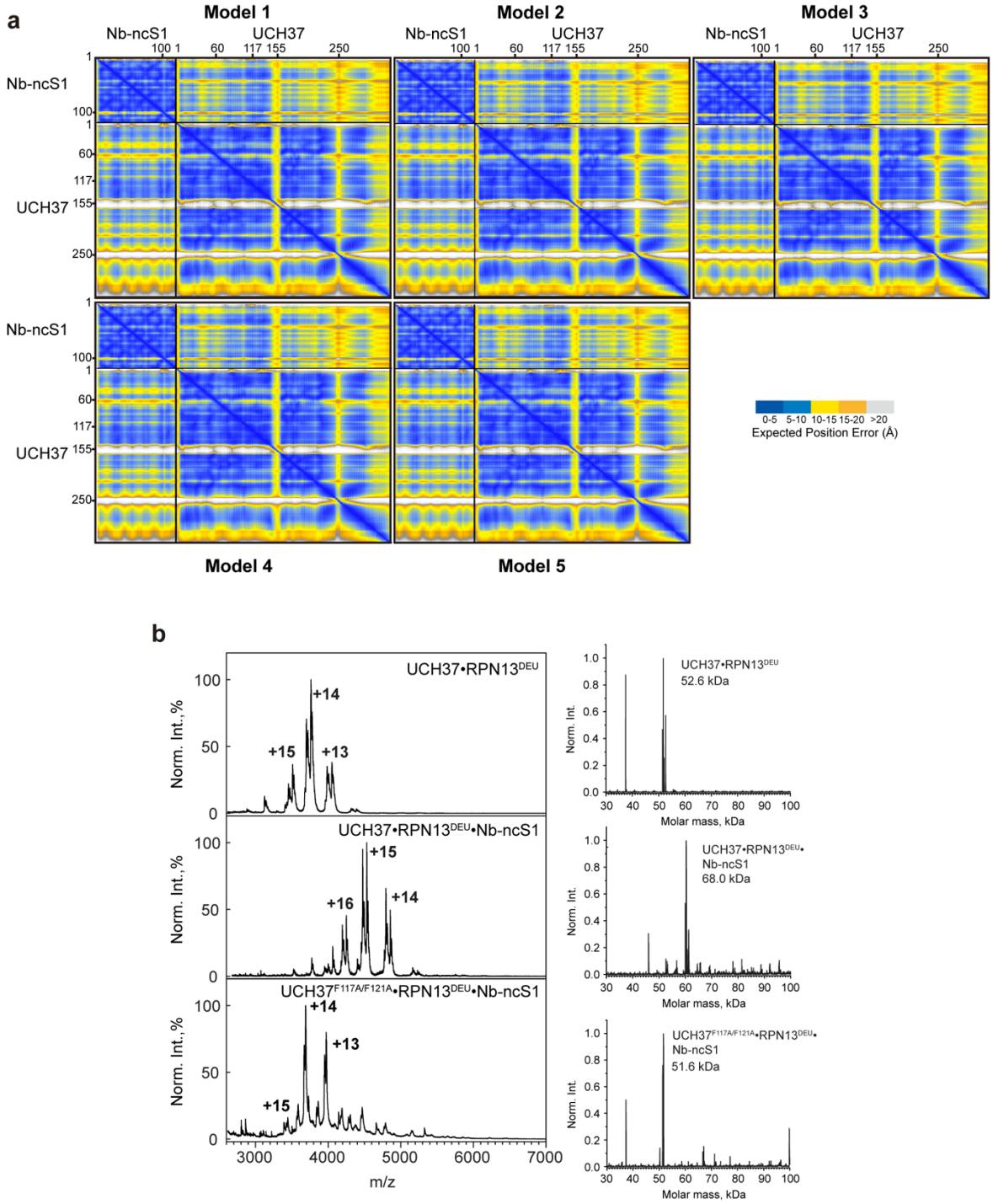

Supplementary Figure 4: Interaction between Nb-ncS1 and UCH37 is Predicted to Occur on the Backside of UCH37.

(a) Predicted Alignment Error (PAE) plots for Nb-ncS1 bound to UCH37. The x- and y-axes correspond to residue indices for Nb-ncS1 and UCH37. Colors indicate the expected positional error (in Å) at residue *x* when the predicted and actual structures

are aligned at residue *y*, with blue representing high-confidence alignment (low error) and lighter colors to orange/gray indicating lower confidence (higher error).

(b) Native ESI-MS spectra of free UCH37•RPN13^{DEUBAD} (top panel), Nb-ncS1-bound UCH37•RPN13^{DEUBAD} (middle panel), and Nb-ncS1 bound to Ub-UCH37$^{F117A/F121A}$•RPN13^{DEUBAD} (bottom panel). Additional peaks observed in the +13 to +15 charge states for free UCH37•RPN13^{DEUBAD} and in the +14 to +16 charge states for the complex correspond to N-/C-terminal truncations in the DEUBAD domain of RPN13. Deconvoluted spectra corresponding to each raw trace are shown to the right.

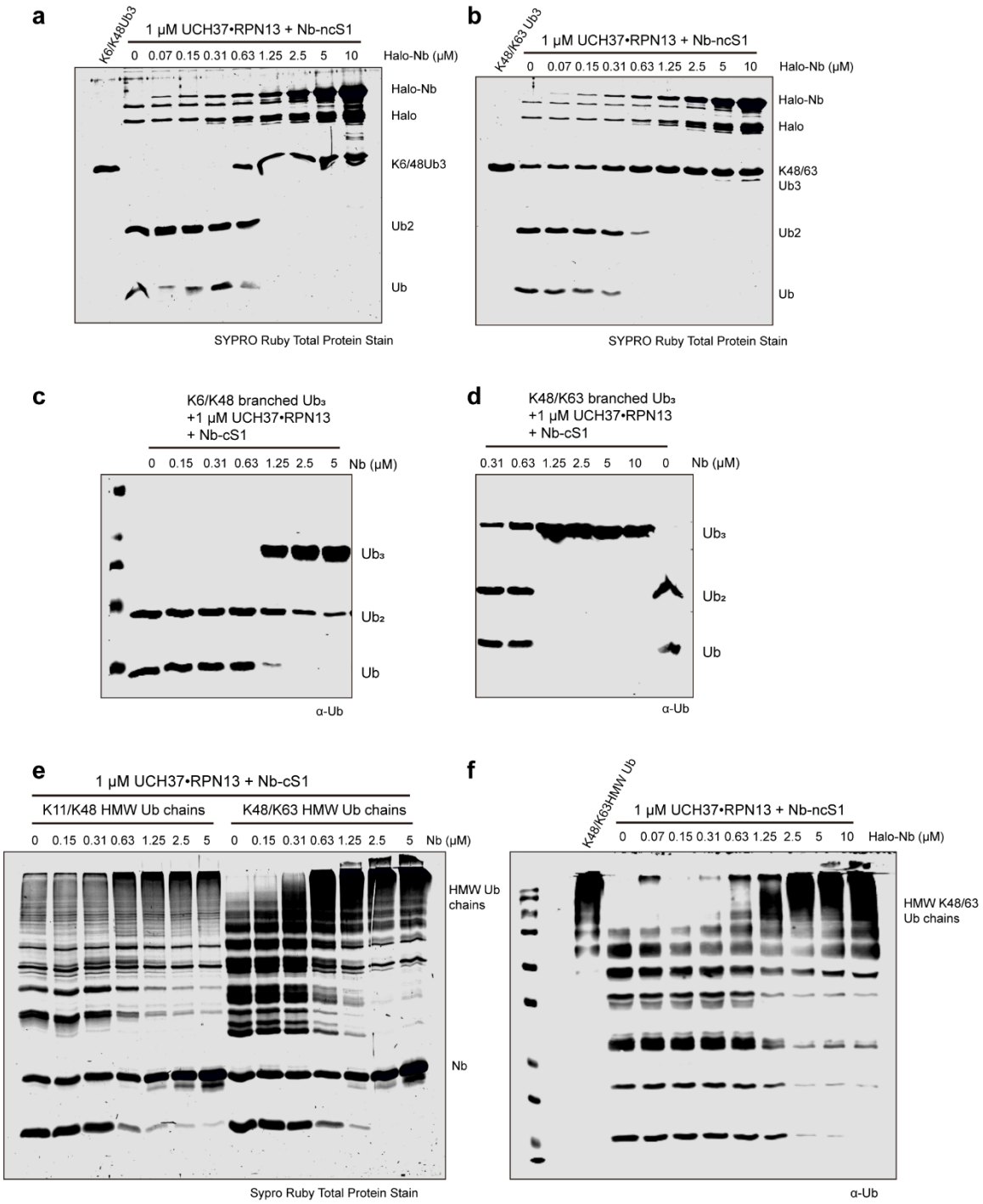

Supplementary Figure 5: Nb-ncS1 and Nb-cS1 Both Inhibit the K48 Debranching Activity of UCH37

(a-b) SDS-PAGE analysis of the cleavage of K6/K48 (a) or K48/K63 (b) branched trimer with 1 μM of UCH37•RPN13 co-incubated with different concentrations of Halo-tagged Nb-ncS1.

(c-d) Western blot analysis of the cleavage of K6/K48 (c) or K48/K63 (d) branched trimer with 1 μM of UCH37•RPN13 co-incubated with different concentrations of Nb-cS1.

(e) SDS-PAGE analysis of the cleavage of K11/K48 or K48/K63 high-molecular weight (HMW)

Ub chains with 1 μM of UCH37•RPN13 co-incubated with different concentrations of Nb-cS1.

(f) Western blot analysis of the cleavage of K48/K63 high-molecular weight (HMW) Ub chains with 1 μM of UCH37•RPN13 co-incubated with different concentrations of Halo tagged Nb-ncS1.

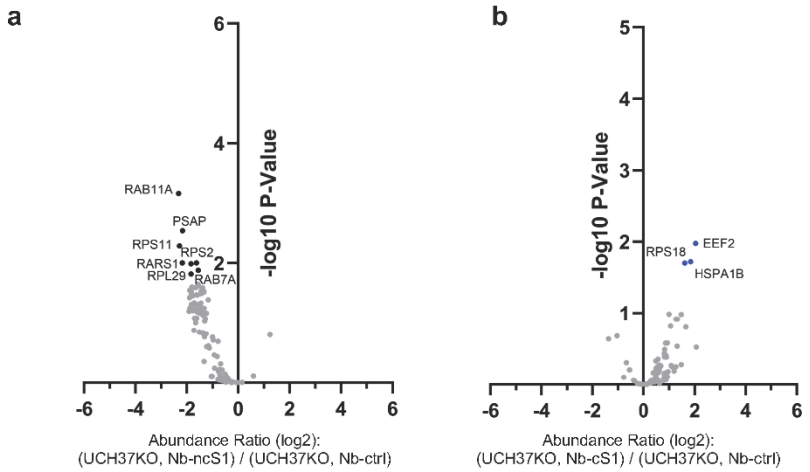

Supplementary Figure 6: Nb-ncS1 and Nb-cS1 Did Not Pull-Down Proteasome in UCH37KO Cells

(a-b) Volcano plot from IP-TMT-MS data comparing proteins enriched by Halo-tagged Nb-ncS1 (a) or Halo-tagged Nb-cS1 (b) versus the Halo-tagged control nanobody (Nb-ctrl).

Primers	Sequence (5'-3')
a1_f	GCTAGCCAGGTGCAGCTGCAGGAAAGCGGCGGCGGCCTGG TGCAGGCGGGC
a2_r	GCCGCTCGCCGCGCAGCTCAGGCGCAGGCTGCCGCCCGCC TGCAC
b3_f	CGCGGCGAGCGGCWMTATTTYTNNKNNKNNKNNKATGGGCT GGTAT
b4_r	AATAGYAGCAACAAGTTCGCGTTCTTTGCCCGGCGCCTGGCG ATACCAGCCCAT
c5_f	GTTGCTRCTATTRVTNNKGGTRSTANTACCWATTATGCGGATA GCGTGAAAGGCCGCTTT
c6_r	TTCATCTGCAGATACACGGTGTTTTTCGCGTTATCGCGGCTAA TGGTAAAGCGGCCTTT
d7_f	TCTGCAGATGAACAGCCTGAAACCGGAAGATACCGCGGTGTA TTATTGCGCGG
d8_short_r	CCCCAATATGCAWRMNNMNNMNNMNNMNNARCCGCGCAATA AT
d8_medium_r	CCCCAATATGCAWRMNNMNNMNNMNNMNNMNNMNNARCCG CGCAATAAT
d8_long_r	CCCCAATATGCAWRMNNMNNMNNMNNMNNMNNMNNMNNMN NMNNARCCGCGCAATAAT
e9_f	GCATATTGGGGCCAGGGCACCCAGGTGACCGTGAGCAGCGG TGGTGGTGGTAGC
e10_r	GTCCCCGAAGTTCAGACCGGTGCTACCACCACCACCGCTGCT CACGGT
pCT_nb_PstI_f	GGTGGTGGTTCTGCTAGCCAGGTGCAGCTGCAGGAA
pCT_nb_Bam HI_r	TTACAAGTCCTCTTCAGAAATAAGCTTTTGTTCGGATCCGCTAC CACCACCGCT

Supplementary Table 1: Primers Used in the Generation of the Nanobody Library

Nb variants	Sequence
Nb-v1	QVQLQESGGGLVQAGGSLRLSCAASGYIFRSYRMGWYRQAPGKE RELVAAIGLGGNTYYADSVKGRFTISRDNAKNTVYLQMNSLKPEDTA VYYCAALHGKPPAFSPFAYWGQGTQVTVSS
Nb-ncS1	RVQLQESGGGLVQAGGSLRLSCAASGYIFRSYRMGWYRQAPGKE RELVAAIGLGGNTYYADSVKGRFTISRDNAKNTVYQQMNSLKPEDT AVYYCAALYGKPPAFSPFPYWGQGTQVTVSS
Nb-v2	QVQLQESGGGLVQAGGSLRLSCAASGYISRPRTMGWYRQAPGKE RELVATISNGAITNYADSVKGRFTISRDNAKNTVYLQMNSLKPEDTAV YYCAAGKNIWHAYWGQGTQVTVSS
Nb-cS1	QVQLQESGGGLVQAGGSLRLSCAASGYISRPRTMGWYRQAPGKE REFVAIISNGAITNYADSVKGRFTISRDNAKNTVYLQMNSLKPEDTAV YYCAAGRNIWHAYWGQGTQVTVSS
Nb-ctrl	QVQLQESGGGLVQAGGSLRLSCAASGSISKWGLMGWYRQAPGKE RELVAAIDSGANTYYADRVKGRFTISRDNAKNTVYLQMNSLKPEDTA VYYCAVVAIRRSDHADWGQGTQVTVSS

Supplementary Table 2: Sequences of the Nanobodies

UCH37 – RPN13 DEU Nb-cS1	
Data Collection and Processing	
Beamline	APS GM/CA 23-ID-B
Resolution range (Å)	37.3 – 2.4 (2.49-2.40)
Space group	$C222_1$
Cell dimensions	
a, b, c (Å)	45.56, 178.63, 190.73
α, β, γ (˚)	90, 90, 90
Total reflections	99575 (10358)
Unique reflections	29105 (2823)
Redundancy (%)	3.4 (3.7)
Completeness (%)	94.58 (94.16)
R_{merge}	0.066 (0.831)
R_{meas}	0.079 (0.978)
R_{pim}	0.043 (0.508)
I/σ(I)	14.72 (1.62)
CC1/2	0.998 (0.532)
Wilson B ($Å^2$)	68.85
Refinement	
Complex/A.S.U., Complex Ratio	1, 1:1:1
Resolution (Å)	2.40
Rwork / Rfree	0.235 / 0.271
No. nonhydrogen atoms	3770
Protein	3701
Water	65
Chloride ions	4
B factors ($Å^2$)	87.58
Protein	87.74
Water	77.99
Chloride ions	95.50
R.m.s.d	
Bond lengths (Å)	0.003
Bond angles (˚)	0.59
Ramachandran (favored/allowed/outliers)	94.9 %, 5.1 %, 0 %
Clash score	8.01

Supplementary Table 3: Data collection, processing, and refinement statistics for the X-ray crystal structure of UCH37 RPN13 DEUBAD complex bound to Nb-cS1. Data is deposited in the Protein Data Bank under the accession code 9E7K.